Experimental and Numerical Investigation of the Mechanical Behavior and Morphological Characteristics of 3D Printed Materials Made via Fused Deposition Modeling (FDM)

Kuotian Liao

A thesis
submitted in partial fulfillment of the
requirements for the degree of

Master of Science in Aeronautics and Astronautics

University of Washington

2021

Reading Committee:

Marco Salviato, Chair

Jinkyu Yang

Program Authorized to Offer Degree:
William E. Boeing Department of Aeronautics and Astronautics

University of Washington

Abstract

Experimental and Numerical Investigation of the Mechanical Behavior and Morphological Characteristics of 3D Printed Materials Made via Fused Deposition Modeling (FDM)

Kuotian Liao

Chair of the Supervisory Committee:
Marco Salviato

Over the past two decades, Additive Manufacturing (AM) as a mean of production has seen rapid growth in adoption across a wide spectrum of industrial sectors. While additively manufactured materials are commonly inferior in strength than those same materials manufactured using traditional methods, the many inherent advantages of AM still make it an appealing alternative to traditional manufacturing methods. Among all the AM techniques, Fused Deposition Modeling (FDM) has been one of the most popular AM technologies fielded by the industry. With the introduction and popularization of high performance thermoplastic feedstocks, FDM is being explored as a viable option for fabrication of load-bearing components in end-use products.
The focus of this thesis is in developing a morphological characterization package based on digital image analysis to analyze the microstructure of FDM additively manufactured materials, and to adapt a discrete finite element model developed by Antonio Deleo at MAMS lab UW to capture their mechanical behavior under uniaxial tensile loading as a function of the print directions. This thesis is the first part of a multi-stage process aimed at developing a complete, physics based guideline for the design of FDM manufactured components, laying down the groundwork for future studies.

TABLE OF CONTENTS

LIST OF FIGURES

LIST OF TABLES

ACKNOWLEDGMENTS

First of all, I wish to thank professor Marco Salviato for his guidance and mentorship as PI over the past four years, and for financially sponsoring the expense of this thesis. I also wishe to thank professor Jinkyu Yang for his mentorship over the past two years, and especially for his unreserved support during crucial times of need. I would like to thank Dr. Yao Qiao for his mentorship over the past four years at MAMS Lab, and Antonio Deleo for his support and assistance in completing this thesis. I also want to express my gratitude to William Kuykendall and Tatyana Galenko for their supports in conducting the experiments during this thesis. Lastly, I would like to thank the Department of Aeronautics and Astronautics and the Theodore H. and Marie M. Sarchin Endowed Fellowship in Engineering for financially supporting my study over the past two years.

Chapter 1

INTRODUCTION

1.1 An Overview to Additive Manufacturing

Additive Manufacturing (AM), more commonly known as 3D-printing, is a manufacturing technology for constructing three-dimensional objects via the direct deposition of feedstock materials [1]. Typically, the materials are deposited in layers, with each successive layer bonding to the previous one, stacking up to form the desired object in three dimensional space [2]. Due to this nature of AM, the interface between layers is usually weaker than the bulk material itself [3]. Depending on the type of AM, there can be weak spots within each layer as well. As a result, AM structures are typically anisotropic and are of inferior strength to their counterparts manufactured using traditional manufacturing methods. However, there are also many advantages that are inherent to AM, such as the ability to achieve highly intricate forms in finished product, the option to optimize part design, and to reduce the number of parts by combining them into a single, continuous component with very little penalty in manufacturing time and difficulty. Furthermore, AM enables the reduction of material wastage compared to traditional manufacturing while providing flexibility in manufacturing by being able to use the same equipment for different manufacturing goals without the need to change tooling or configuration [1]. To summarize in one sentence: in the world of AM, complexity is "free".

First emerged in 1984, AM technologies have gone a long way [4]. The earliest commercialized AM methods such as Stereolithography Apparatus (SLA) [4] and FDM [4] were mainly designed for polymers. At the time, AM was regarded as a method for prototyping and not much more. This is partly due to the lack of high per-

(a) Turbine blade made with metal AM (Siemens)

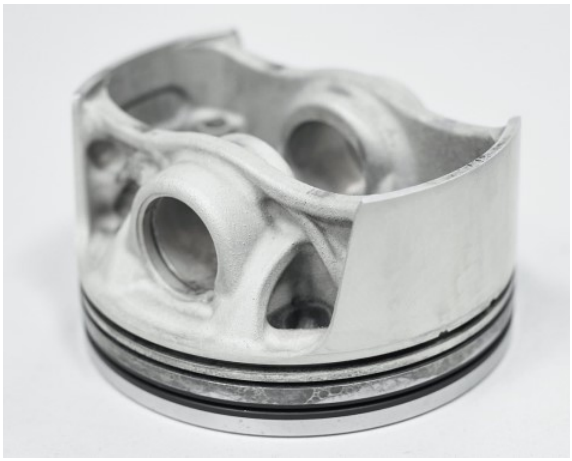

(b) Engine piston made with metal AM (Porsche)

(c) 3D-printed polymer engine intake manifold (Windform)

(d) Part repair using polymer AM (Tesla)

Figure 1.1: Examples of end-user parts made using AM

formance feedstock materials at the time, and the reduced strength compared bulk materials resulted from inherent interlaminar and intralaminar weak spots in additively manufactured materials. However, the strength that additively manufactured

materials are able to achieve has improved over time. This is partly thanks to the development in new methods of AM for metals such as Powder Bed Fusion (PBF) and Directed Energy Deposition (DED), and partly thanks to the development of new, stronger polymer-based feedstocks such as Polyether Ether Ketone (PEEK) and various Fiber-Reinforced Plastics (FRP) for existing AM techniques such as FDM [4, 1]. The strength gap between additively manufactured materials and conventionally manufactured materials has narrowed to a point, where this deficit can be out-weighed by other inherent advantages of AM [5]. As a result of these innovations, AM has been used more and more extensively on end-use products. Some examples of AM being used for end-use products are shown in figure 1.1.

1.2 An Introduction to the Fused Deposition Modeling (FDM) Method

Fused deposition modeling is an extrusion-based AM method by which a feedstock material is extruded via a nozzle, laying down material following a predefined path in a controlled manner [1]. This simple operating principle behind FDM systems allows it to be used with a wide range of materials for almost any application. FDM type AM systems be seen in a wide range configurations from low end units designed to use common thermoplastics such as ABS and PLA, to high end apparatuses that uses high performance materials such as PEEK and FRPs [1, 6].

For typical polymer FDM systems, the operating principle is fairly standard across the board. The feedstock material is first melted, before being extruded through said nozzle, laying down material along a path and forming a"filament" [1]. Each fresh filament, while still in a melted state, will bond with both adjacent filaments within the same layer, and filaments from the previous layer before it cools down and solidifies completely [1].

Although polymer FDM systems that uses solid feedstock are the most commonly seen variant, there are specialized systems designed to use feedstock in near-liquid or gel-like consistency (usually requires post-print curing process) that share the same

principles as FDM (extrusion based operation) [7]. These type of "pseudo-FDM" systems are typically designed for the medical industry to be used with hydrogel based "bio-inks" [7].

Advantages of FDM systems compared to other polymer AM systems such as SLA include the relatively simple post-processing procedures, a wider selection of available feedstock materials, and most importantly, the ability to scale any given system relatively inexpensively [8]. This is because the only hard limiting factor to the scale of an FDM type system is the size of the frame where the extrusion assembly resides. The frame can be expanded or shrunken easily to accommodate systems of different sizes without much alternation needed for the "core" components such as the extrusion assembly.

1.3 Advantages and Limitations of FDM for Structural Applications

One major challenge in designing for FDM is the anisotropy of the printed material, whose physical properties are primarily determined by the print direction of each layer and their stacking sequence. This is a direct result of the FDM operating principles, as filaments that are extruded will inevitably have rounded corners, forming voids between filaments, as illustrated in figure 1.2 [9, 10]. However, with understanding in the physical characteristics introduced by such anisotropy in the printed material, we can utilize it in our favor. In fact, mother nature is full of examples of anisotropic materials generated by animals. For example, the shell of a mantis shrimp consists of strands chitin fibers oriented in a bouligand structure, helping it achieve a high level of toughness that can resists high velocity impact, allowing its claw to safely deliver a punch that can puncture the shells of its prey [11]. With clever programming of the inherent void defects generated in the FDM printing process, we can achieve structural behaviors that would be impossible to accomplish with homogeneous materials [12, 13].

Another limiting factor of FDM in structural applications, also being an inherent

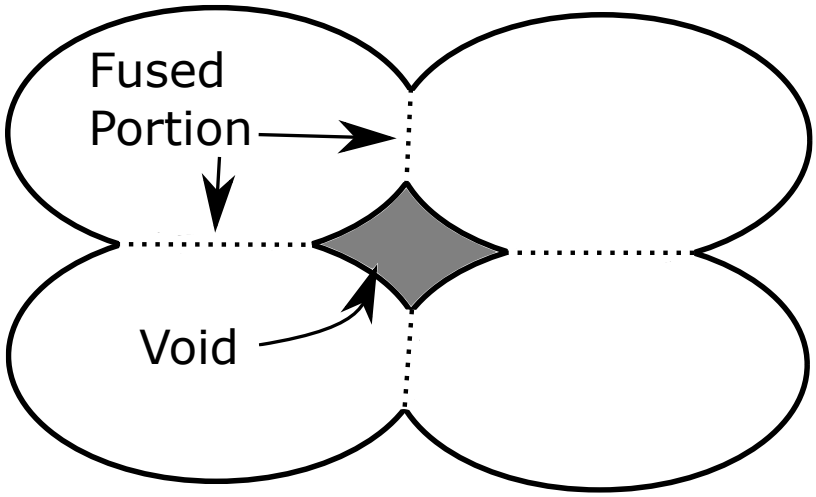

Figure 1.2: Illustration of inter-filament void in FDM printed materials

feature of its operating principles, is the inferior strength compared to same materials of a homogeneous nature [9]. When loading along the printed filaments, this reduced strength is due to the existence of the aforementioned inter-filament voids. This effectively forms a porous structure in the cross section of the printed material, reducing the amount of load-bearing material in a given cross sectional area [9]. When loading along directions not aligned with the filament direction (either transversely in-plane or out-of-plane), the strength deficit is the combined result of both the inter-filament voids and the reduced strength at bonding surfaces between filaments (in-plane and out-of-plane) when compared to the bulk material [9].

1.4 Proposed FDM Design Guideline and Project Overview

Although many researchers have studied FDM in the past, there still lacks a definitive, physics driven guideline that can provide quantitative directions for designers to utilize FDM in structural applications [6, 3, 14, 15]. Therefore, it is the vision of us at MAMS lab UW to provide a set of comprehensive design guideline that can be used in industries for designing FDM manufactured components with load-bearing intentions.

We know that the FDM printed material has a mesostructure that is formed by the printed filaments and the inter-filament voids. This mesostructure can be altered by printing parameters and it in turns will dictate the mechanical performance in the printed structure. The key to developing a comprehensive design guideline is in bridging the gaps between the printing parameters, mesostructure and material performances. To realize this vision, we are proposing a four-stage approach:

1. Developing a quick and robust method for analyzing and quantifying the mesostructural morphological characteristics of FDM printed materials.

2. Establishing a correlation between printing parameters (software settings + machine configurations) and morphological characteristics of the printed material using the analysis method developed in step 1.

3. Developing a numerical model that is able to simulate the mechanical behaviors of FDM printed materials when given mesostructure measurements.

4. Calibrate the numerical model developed in step 3 using selective mechanical testing results. Once calibrated, the model should be able to predict the mechanical properties of FDM printed structures of different printing directions and geometries (that share the same printing parameters as the calibration samples).

A road map of this proposed four-stage approach is shown in figure 1.3.
Due to the time limit of my program, the focus of this thesis was on stage 1 and stage 4. A discrete FEM model already developed by our group at MAMS was selected and adapted to fill stage 3. The first major goal of this study was to develop a robust and efficient approach for analyzing the morphology characteristics of FDM 3D-printed materials at the mesoscale through optical microscopy samples. The second major

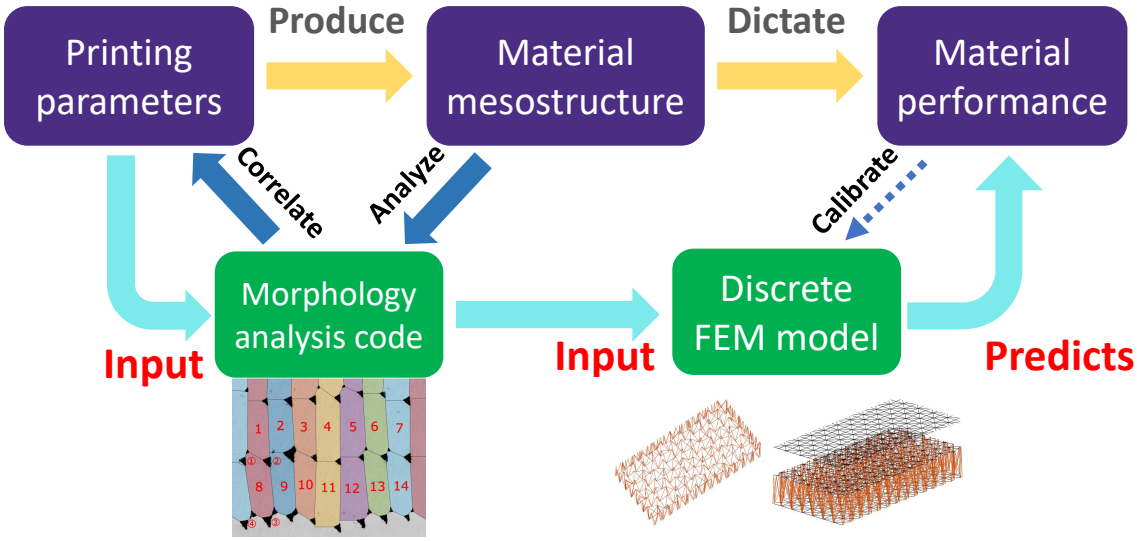

Figure 1.3: Road map visualizing proposed FDM design guideline

goal was to validate an existing Finite Element (FEM) model developed by MAMS for capturing the mechanical behaviors of FDM 3D-printed materials

To achieve the first goal, I have developed and implemented a morphology analysis package in Matlab. To validate its capability, I used the package to analyze cross-section microscopy images of an FDM 3D-printed sample. To achieve the second goal, I first characterized the mechanical properties of our FDM 3D-printed material from mechanical testing results. Then, I modeled the tested samples using our in-house FEM model and calibrated the model to capture these material properties.

Chapter 2

DESIGNING AND MANUFACTURING FDM SPECIMENS

2.1 Choosing Print Quality Target

At the onset of the project, I was a relative novice to FDM 3D-printing and AM in general. Therefore, the first target was to experiment and choose a set of printer settings that generates a decent enough print quality, which will be kept for the remainder of this project. As different printer settings and their effect on the printed structures are not the focus of this project, I simply followed the guidelines from the printer manufacturer and online forums to determine whether my print is of "good quality" [16].

The initial criteria by which I determine a "good quality print" is listed below. As the project progresses, more criteria have also been added to this list. These new criteria will be discussed later in this chapter.

- Even width of extruded filaments within each layer.
- No overflowing of material around the edges at each layer.
- No distortion to the overall shape of the printed part.
- No stringing between printed parts when printing multiple parts at once.
- At 100% infill, there should be neither overlapping filaments nor gaps between filaments within each layer.

2.2 Printing Parameters Configuration: Overview

The printer used in this project was a *Prusa i3 Mk2 Multi-Material* 3D printer (shown in fifure 2.1). It is a hobby grade FDM 3D printer that is designed to work with most common thermoplastic polymers such as ABS, PLA, PP, PC, etc. We chose it because we have already have it in the lab, and it shares the same FDM operating principles as much more expensive systems that utilizes high performance material such as PEEK, which our group will eventually work with in the future.

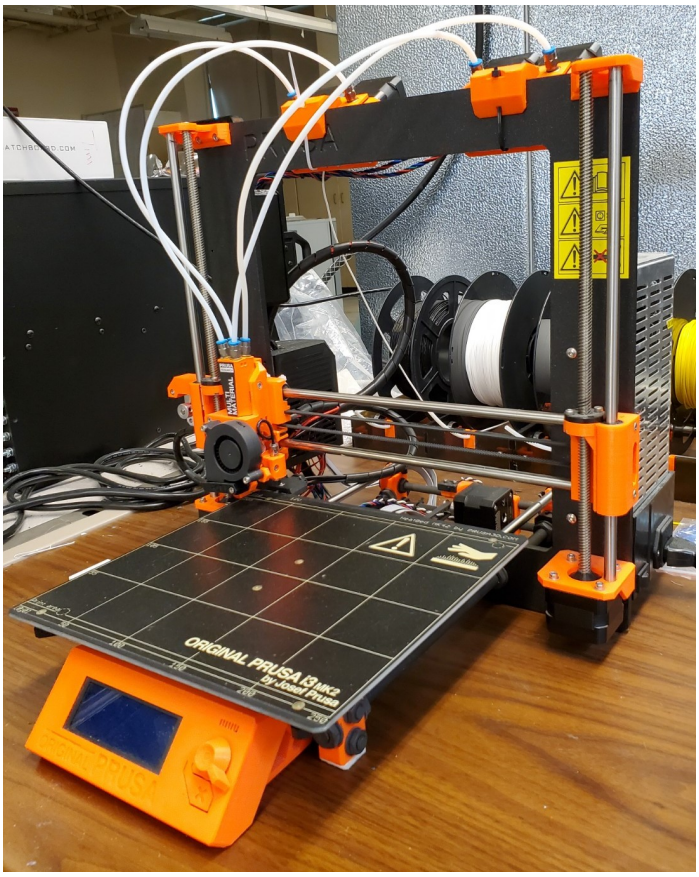

Figure 2.1: Prusa i3 Mk2 printer used for this project

Generally speaking, after modeling the object to be printed in a CAD software such as SolidWorks, a pre-processing software commonly known as a "slicer" is required to

turn the 3D object file into commands that can be executed by the printer. The slicer software that I used throughout the project was *Ultimaker Cura*, which I chose over the *PrusaSlicer*, the slicer developed by the manufacturer of our printer. I chose the *Ultimaker Cura* software mainly because it provides a lot more customizable options that are easy to access than the *PrusaSlicer*, which is very useful for dialing in the "good quality" for this project. The abundance of customizable settings will also be an important asset for future students who are going to attempt correlating printing parameters to morphological characteristics.

The material we selected for this project was PLA, because it is easy to print, inexpensive and even shares some of the characteristics with PEEK. Although much weaker in both strength and elastic modulus when compared with PEEK, PLA is similar to PEEK in that they are both semi-crystalline in their crystal structures. The particular brand we chose was *Hatchbox*, because it was the most popular brand on Amazon, which means the availability of the material is not likely to be an issue down the line.

A summary of critical printing parameters used for this project can be seen in table.2.1 below.

Setting Name	Setting Value	Unit
Layer Height	0.15	mm
Line Width (wall & infill)	0.4	mm
Wall Thickness	1	line
Infill Line Distance (density)	0.4 (100%)	mm
Printing Temperature	200	°C
Print Speed	30	mm/s

Table 2.1: Printer Settings

2.3 Print Quality Test and Parameters Re-Configuration

Although the print quality was initially deemed satisfactory from the selected settings shown in table. 2.1. What we had not considered was the effect of the travel moves of the print head over printed parts. Such moves are automatically implemented by the slicer software in the printing process when it attempts to cover the entirety of any layer. These moves cannot be removed from the *Ultimaker Cura* GUI, and the time and place where these moves will take place is entirely determined by the software depending on the geometry of a given layer. If the filament is not retracted back from the nozzle, the residual material in the nozzle will still be deposited and form an unintended trail of material even when the feeding motor is stopped during the travel moves by the print head. This is undesired as it alters the in-plane morphology of each layer and may affect the performance of the printed part if present within the gauge area or otherwise critical regions. We successfully eliminated this residual trail problem by implementing retraction commands, which allows the stock filament to be retracted away from the hot nozzle before each travel move. The retraction distance we settled on at the end was 6mm for the tensile specimens, as it provided the best results. Figure 2.2 shows the comparison between test samples printed without retraction, and ones printed with retraction.

2.4 Machine Repair and Re-Calibration

During the process of the project, the machine had encountered a couple technical issues, with each costing valuable time to debug. To help future students at MAMS avoid similar pitfalls, I will hereby list all the technical problems the printer has had over my stint on the project, and how each of them was finally resolved. One of the first system malfunction was with the bed temperature sensor, which was held in place underneath the bed by aluminum tape. The original tape had degraded over time, and was no longer able to hold the sensor in place. As a result, the bed temperature

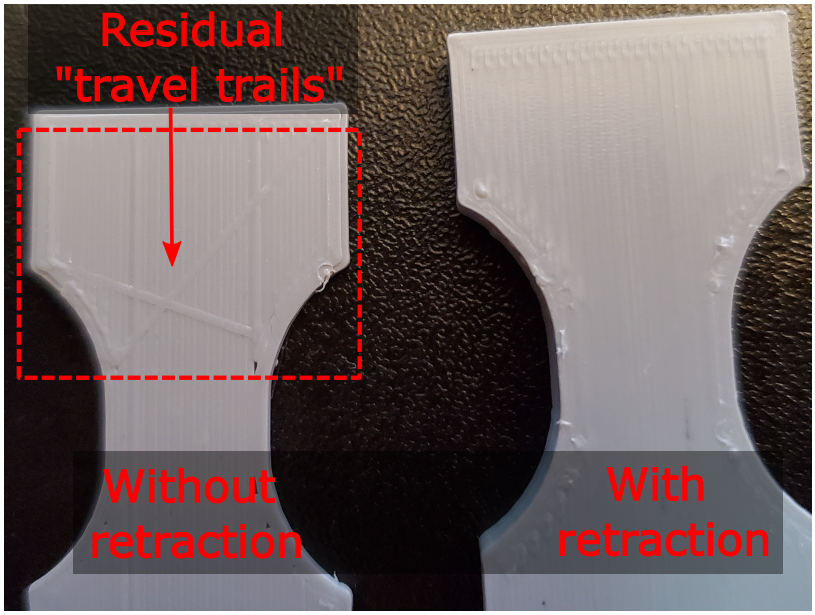

Figure 2.2: Example of the "travel trails" and the effect of retraction

readout would stay at room temperature. This then results in the bed temperature to rise indefinitely, causing the base layers of the print to soften. To try and fix it, I initially only replaced the old tape with new ones but to no avail. At the end, a new sensor was ordered and re-attached to the build plate. Figure.2.3 shows the bed temperature sensor correctly attached to the build plate.

Another major malfunction was due to unknown reasons, but possibly due to a faulty nozzle temperature sensor or a clogged nozzle. As this malfunction happened with no-one monitoring the system, a huge blob of molten plastic had accumulated at the nozzle and on the build plate of the machine by the time someone noticed the problem. Because we could not definitively confirm the source of the problem, we decided to swap out the entire extruder assembly. After the extruder assembly was swapped, a visual print quality examination was conducted to confirm the printed part satisfies all the criteria proposed in Section 2.1 and 2.3.

The change of the extruder had also gone on to cause a significant change in the

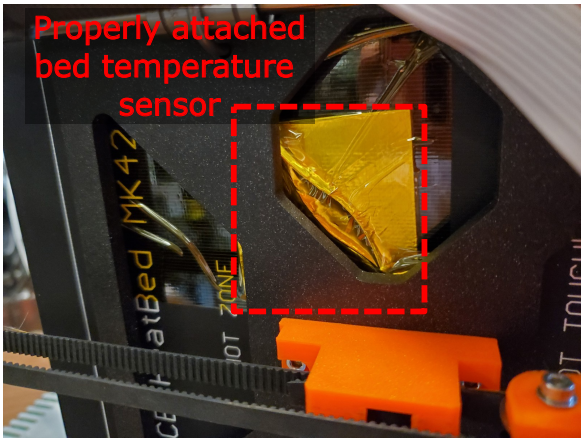

Figure 2.3: Properly attached bed temperature sensor

morphology of the printed parts, even when the same settings were used. But overall, the print quality changed for the better following the extruder change, with much more uniform void shapes and sizes observed as well as a lower void fraction. The comparison of the cross section morphology of the new and old material is shown in figure 4.4. I will further discuss this morphology change in chapter 5 and 6.

As a suggestion to prevent such catastrophic event from occurring again, I strongly recommend anyone who is going to use the 3D printer in MAMS to check on it periodically, and not leave it on a job overnight.

2.5 Case-Specific Parameters Re-Configuration

Although all the print quality criteria were met for the tensile specimens, some issues were observed when printing the Single Edge Notched Bending (SENB) specimens using the same set of printer settings. The problem appears to be the failure to extrude immediately following a travel move with retraction. This phenomenon can be seen depicted in samples shown in figure 2.4, which appears as incomplete lines or gaps between filaments within a layer. Due to time constraints, I was unable to isolate and identify the cause of these defects by altering print settings one at a

time. Instead, I reduced the retraction distance from 6mm to 4mm, and increase initial printing temperature (the lowest possible nozzle temperature at which the print can start) from 190 °C to 200 °C (same as the desired printing temperature). These implemented changes successfully resolved the issue, while still satisfying all the quality criteria described previously in section 2.1 and 2.3.

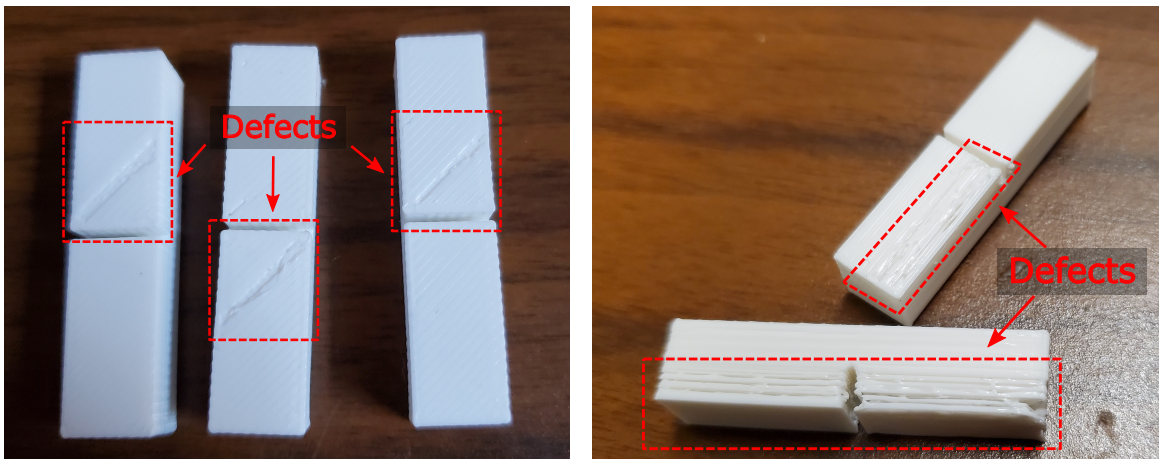

Figure 2.4: Print defects in SENB specimens

Chapter 3

EXPERIMENT DESIGN AND METHODOLOGY FOR MECHANICAL TESTS

3.1 Standard Selection and Specimen Design

To avoid any inconsistency that may be a result of test design, we chose to base all of our test designs on existing ASTM standards. Because existing mechanical testing standards for AM materials are only available for metals, we chose to use the ASTM standards for testing traditional plastic materials. Namely, we based our tensile specimen dimensions on ASTM D638 [17] and chose ASTM D5045 [18] as the guide for our SENB specimens. We also chose to have the dimensions of the specimens be significantly larger than the dimensions of the individual filaments to minimize any possible inconsistency due to size effects. One size of the tensile specimen and two sizes of the SENB specimens were tested.

The dimensions of the tensile specimens are shown in figure 3.1a. The two sizes of the SENB specimens can be seen in figure 3.1b. The spans (L) of the SENB specimens were chosen based on the available fixture dimensions. The overall length of the actual specimens are (L+4mm) in length to allow extra length on either side of the fixture supports. The smaller SENB specimen was scaled down from the larger one in 2 dimensions (W & L), while the height (B) was kept the same. The lengths and size ratio of the SENB specimens were referencing the specimen dimensions previously studied utilizing epoxy-graphene nanocomposites from our group by Mefford et al [19]. A center notch of 1mm width was part of the print for both specimen sizes. The length of the notch is 50% of the specimen width (W/2). In both cases, the print direction is orthogonal to the top face from the three-view diagram (build plane is

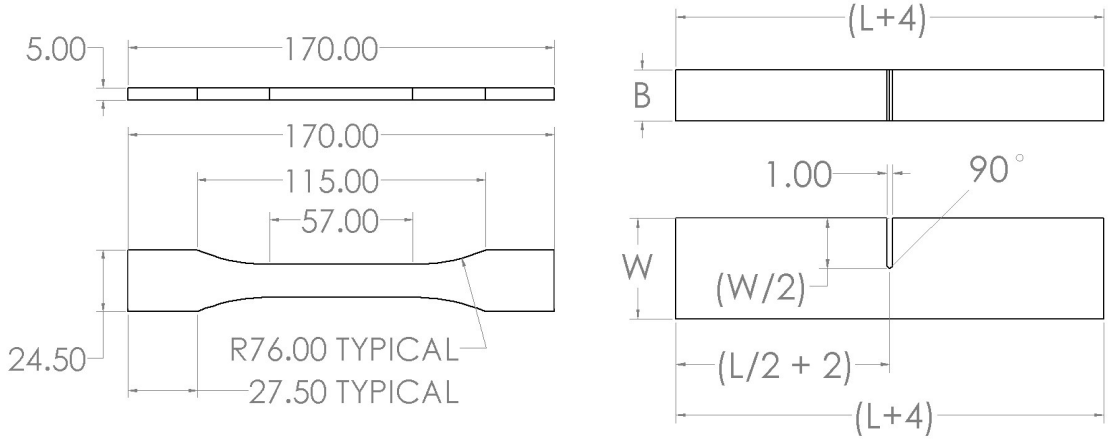

(a) Tensile specimen specification (D638) (Units in mm)

(b) SENB specimen specification (D5045) (Units in mm)

Figure 3.1: Design specifications of specimens used in mechanical tests

aligned with L*B plane for tensile and L*B plane for SENB). The layup sequence in both cases are specified as the 0° angle being aligned with the L dimension of the specimen.

3.2 Testing Equipment Selection and Setup Overview

To perform uni-axial tensile testing on our printed specimens (D638), we chose to use an Instron 5585H load frame (shown in figure 3.2) with a 250kN load cell and manually operated clamps. We chose to use this machine mainly because it was the only machine readily available to us that is capable of handling specimens of our specification at the time of testing.

To perform the single-edge-notched bending tests, we chose to use a Psylotech μTS micro load frame with custom-made 3 point bending fixtures manufactured by members of our lab. This was chosen because the machine is owned by our group, which can be used for free. We did not use it for the tensile testings as we lacked both ap-

propriate grips for our specimens and could not accommodate the size of our tensile specimens.

Figure 3.2: Instron 5585H

In both the tensile and the SENB tests, the load readouts were recorded and saved by the control software of each system. Instead of using a more traditional strain gauge, we used digital image correlation (DIC) to capture the strain and deformation during the tests [20]. A Nikon D5600 camera with a Nikon AF Micro 200mm lense was used to take images at 1 second intervals during the tensile tests on the Instron. Although I attempted to use the same set up during the SENB tests on the micro load frame, the setup was too cumbersome to operate, as shown in figure 3.3a. As a result, a Dino-Lite AM3111 digital microscope was used instead during the SENB tests. Although a drop in resolution was observed, it was still deemed satisfactory for DIC analysis later on.

(a) Attempted camera setup for the μTS

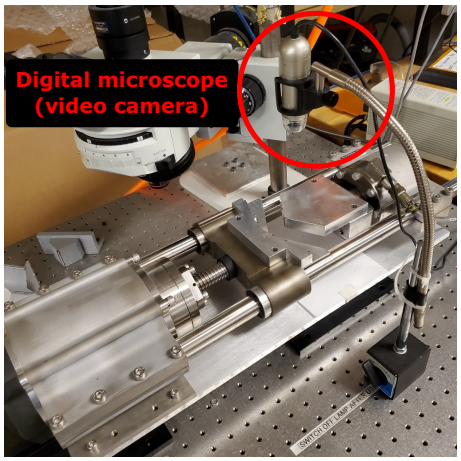

(b) Digital microscope setup for the μTS

Figure 3.3: Camera setup for the μTS micro load frame

3.3 Methodology for Tensile Tests

To capture the anisotropic behavior of the FDM 3-D printed material, the methodology used for mechanical characterization of laminate composite materials was followed [21, 22]. Tensile specimens of 3 different print direction sequences were manufactured for testing. They are $[0]_n$, $[90]_n$ and $[+-45]_n$. Using the uni-axial test results of these 3 layups, the elastic properties $E_1, E_2, G_{12}, \nu_{12}$, and $\nu 21$ as well as the strengths of a lamina can be calculated.

Before the material properties can be calculated, we must first obtain the stress-strain curve from the tensile testings. Equation 3.1, where P is the force recorded during testing, and A is the nominal cross section area taken in the gauge section of the tensile specimen.

$$\sigma = \frac{P}{A} \tag{3.1}$$

The strain values in the gauge area were extracted using DIC. The software we chose for this project was *Ncorr*, a free, open source DIC package designed to work in

Matlab that was developed by Justin Blaber from Georgia Institute of Technology [23]. The software outputs the strain values within the ROI selected as matrices. To calculate the strain values for our stress-strain curve, 2 lines were selected within the gauge area away from any stress concentration, and the average of strain values along those 2 lines were calculated. Because the DIC images were taken at a 1 Hz frequency and the load data from the Instron was logged at 10 Hz, additional strain data points were generated between each recorded frame using linear interpolation.

The linear region of the stress-strain curves from our tests was empirically determined to be 10 seconds before any form of softening takes place.

The longitudinal Young's modulus of the lamina E_1 was calculated based on the slopes in the linear region of the 0°stress-strain curves. Similarly, the transverse modulus E_2 was based on the 90°results. To calculate the shear properties, the ASTM standard for calculating the shear properties of fiber reinforced composite materials was used (ASTM D3518) [22]. The standard states that for uni-axial tensile tests using $[+-45]_n$ laminates, shear properties can be calculated using equation 3.2, where ϵ_x and ϵ_y are the longitudinal and transverse strains from the tests, and τ_{12} is the calculated shear stress.

$$\gamma_{12} = \epsilon_x - \epsilon_y; \qquad \tau_{12} = \frac{P}{2A}; \qquad G_{12} = \frac{\Delta\tau_{12}}{\Delta\gamma_{12}} \tag{3.2}$$

Because both the 0°and the 90°tests exhibited softening following the linear region of the stress-strain curves, both the yield stress σ_y and the ultimate stress σ_u were calculated. The yield stress was determined using the 0.2% plastic strain method.

3.4 Methodology for SENB Tests

The main mechanical property we want to obtain from the SENB tests is the fracture energy of different print layups.

Because our SENB specimens are printed from scratch, the notch in each specimen was designed as part of the print rather than machined a posteriori, which is the

method specified in ASTM D5045 for creating notches in non-additively manufactured specimens [18]. A sharp crack tip beyond the tip of the notch was created on each specimen by tapping a razor blade into the notch [24]. A crack length (beyond the tip of the notch) of 0.5mm was the target for the smaller specimens (L = 36mm), and a crack length of 1mm was aimed for on the larger specimens (L = 72mm). The actual crack lengths (total length measured from the mouth of the notch to the tip of the pre-crack) were measured after the tests.

To calculate the fracture energy G_f, equation 3.3 was used, where $\int_0^{x_f} P\,dx$ is the area under the load-displacement curve, x_f is the load head displacement at fracture, and A_c is the cross-section area of the specimen in front of the crack tip [25].

$$G_f = \frac{\int_0^{x_f} P\,dx}{A_c} \tag{3.3}$$

However, due to the limit posed by our 3 point bending fixture dimensions, we could not actually test the SENB samples to complete failure (break in two). Therefore, a "predicted" fracture energy value may be calculated using artificially extended load-displacement curves. We can then compare the fracture energy values calculated from actual load-displacement curves to the ones calculated from the extended load-displacement curves to estimate the possible error in our calculated fracture energy values.

Chapter 4

CROSS-SECTION MORPHOLOGY STUDY PREPARATION

4.1 Microscopy Sample Preparation

In order to capture the morphology of a 3D printed microstructure for analysis, we chose to use the optical microscopy approach, as it is one of the most commonly used method for analyzing the cross section of fiber composite laminates, and have been used by many previous researchers on 3D-printed materials.

To prepare samples for the microscope, a series of preparation processes were observed. This is based on the method previously used by our group to prepare carbon fiber composite microscopy samples.

First step was to create a cross section in a 3D printed sample. Because the goal of the morphology analysis is to analyze the structure of the printed material before any damage had occurred, it should be obtained either from cutting a pristine printed part, or by cutting away from the gauge area and stress concentrations on a sample that has been tested to failure. For this project, the samples were cut using either a electric band saw or a hand saw. Both methods would create a very rough cut surface, from which a significant layer of material (relative to what would be removed if the cut surface were relatively smooth) would have to be removed.

The second step was mounting the sample in epoxy, forming an epoxy block or puck. This is done to increase the size of the surface that will later be polished, so it is easier to be kept flat against sand papers or polishing wheels later on. for the narrower samples, metal or plastic holders were used to keep them upright in their molds during the pouring of the epoxy.

The third step was the sanding. Because of the need to remove excess material (both due to the rough cut surface of our samples, and the excess epoxy that seeps underneath the samples during mounting) "quick and dirty", I always do a quick dry sanding using a rough grit (65 or 100 grit) before proceeding into finer sanding and polishing. After dry sanding, I would perform wet sanding using a series of finer sand papers of progressively finer grits, up to 2000 grit. Wet sanding was performed on special sanding platforms with running water (figure 4.1a), using a uni-directional technique (only pressing on the down stroke away from body), and turning the sample by 90°for each grit count. Between each grit count, the samples would be quickly examined visually under an optical microscope to ensure the uniformity of the sanding marks from the previous stint. A uniform sanding pattern running in a single direction means sanding on the current grit is sufficient and the sample is ready to move on the next grit count. A non-uniform sanding pattern in a single direction usually means the slight change in angle over a number of strokes due to human error. This is non-critical, and the sample is safe to proceed to the next grit count. However, a crisscrossing sanding pattern means the sample has not been sanded sufficiently on the current grit, with marks from the previous stint still showing through. In this case, more time on the current grit would be needed.

Lastly, the sample would be polished on a polishing wheel (figure 4.1b) with polishing compounds. Polishing slurry at 3 μm and 0.5 μm diameters were used progressively for this project. All the polishing was done by hand for this project. My manual polishing technique was to slide the samples on the polishing wheel opposite to the spinning direction of the wheel itself. This is aimed to achieve the opposite effect as the sanding technique. By sliding the puck across a spinning wheel, the abrasive particles are allowed to polish the target surface from in all direction, which is more efficient for removing sanding marks from the previous step.

At the end, the polished surface should have a smooth, glossy and shiny appearance similar to glass upon visual inspection, and should show very little scratch marks

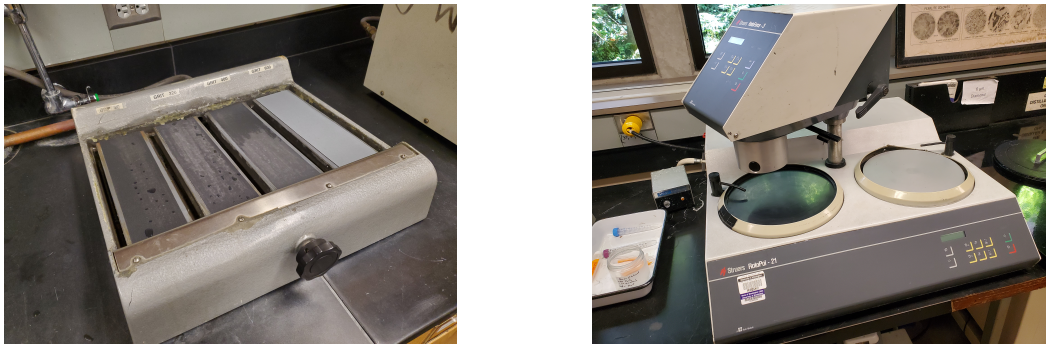

(a) Sanding station

(b) Polishing station

Figure 4.1: Camera setup for the μTS micro load frame

under a microscope.

4.2 Morphology Characterization Method

The shape of inter-filament voids present in FDM 3D printed material has been studied and discussed by many researchers before [26, 27, 28, 10, 3]. In most previous studies, the ideal shape of extruded filaments are characterized as flattened ovals, with the voids that are formed between any four neighboring filaments taking the shape of a diamond with concave edges, as shown in figure 4.2 and 4.3a. However, most previous studies have also confirmed that the shape of actual voids are not rhombic like the ideal void shape, and instead takes the form of either an inverted triangle/kite as shown in figure 4.3b (with print layering direction pointing up towards the top of the page) [26, 27], or a upright triangle/kite as shown in figure 4.3c [28, 10, 3].

Our microscopy studies yielded two different kinds of results before and after the replacement of the extruder assembly on our 3D printer. After replacing the extruder assembly, the shapes of most of the voids in our print can be closely resembled by the upright triangle/kite shape, as shown in figure 4.4a. However, the shapes of a significant number of voids in hour print before the extruder replacement could not

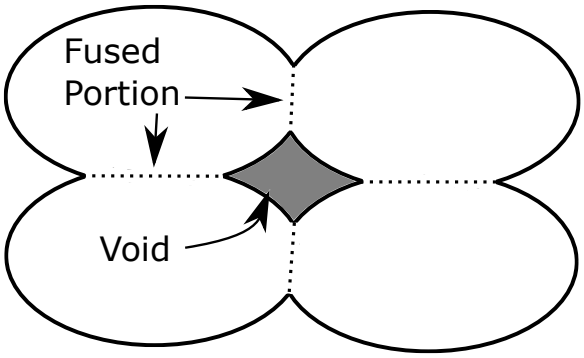

Figure 4.2: Ideal filaments and void

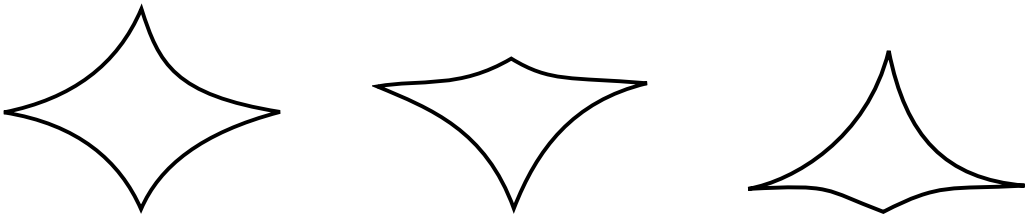

(a) Ideal void (b) Inverted triangle/kite (c) Upright triangle/kite

Figure 4.3: Characteristic void shapes in previous literatures

be well characterized by any of the shapes shown in figure 4.3, as can be seen from figure 4.4b. Therefore, a new characteristic shape was needed to capture the shapes of voids in our early prints.

The shape we proposed to characterize our voids can be described as a “tilted hourglass”, as shown in figure 4.5a. We have also noticed that the filaments diagonally across the void can be fused together in some occasions, distorting the “tilted hourglass” into the “double triangle” as shown in figure 4.5b.

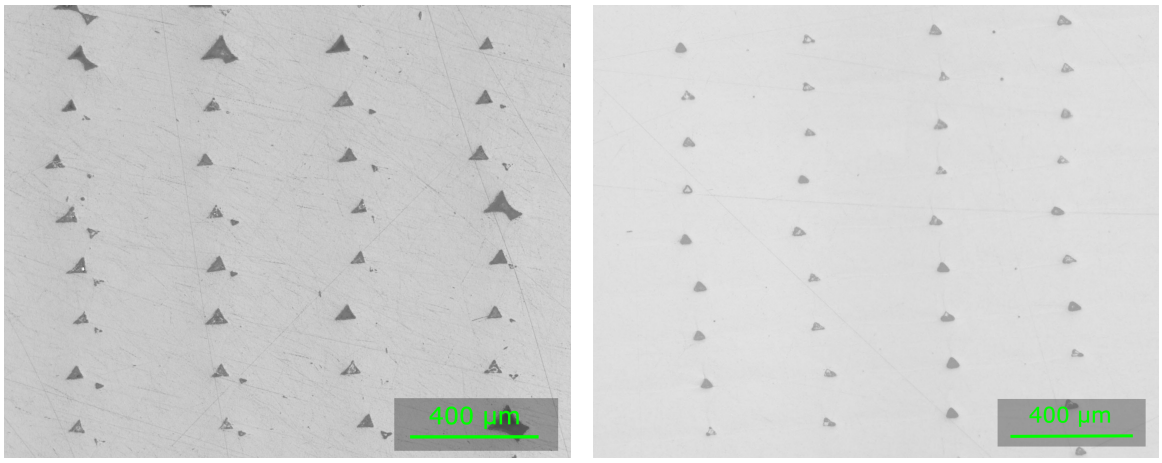

(a) Voids before extruder change (b) Voids after extruder change

Figure 4.4: Comparison of void shapes before and after extruder change

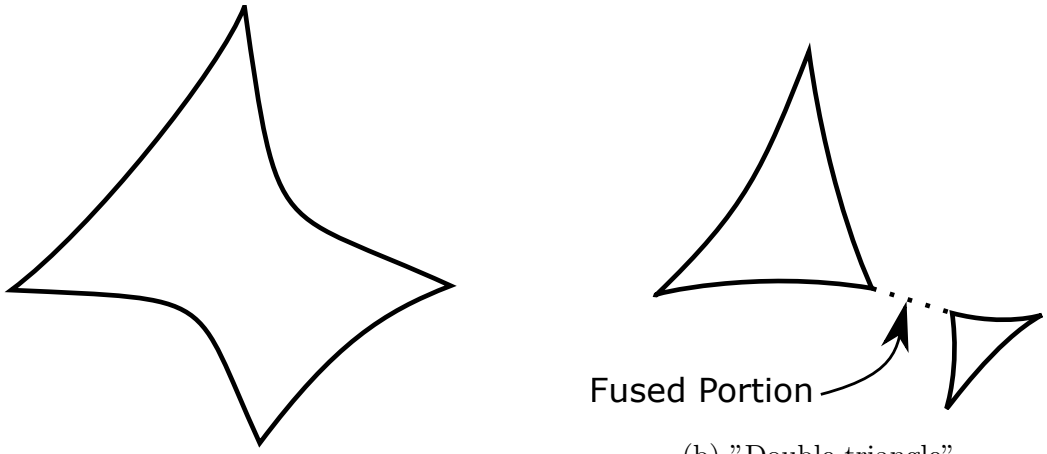

(a) Tilted hourglass/"Merged" (b) "Double triangle"

Figure 4.5: Proposed new characteristic void shapes

4.3 Development of the Void Morphology Characterization Package

4.3.1 Introduction and Overview of Analysis Process

Although there were some previous morphology studies on the voids induced during the FDM manufacturing process, the amount of information presented by these studies were very limited. Most of these studies do not go much further than calculating the area fraction or volume fraction of the voids (from 2D images and 3D scans respectively) [3, 29, 10]. However, as important future steps in completing our proposed FDM design guideline, a complete study in the effect of changing printing parameters on the void morphology of the printed material, and in the effect of changing morphological features on the physical performances of the printed material are both imminent. Therefore, one of the target that we wished to achieve in developing our in-house morphology characterization package was to provide as much detailed information about the shape, size, and other characteristics of the voids as possible. The analysis procedure of our morphology package can be summarized as followed:

1. Pre-processing of the stock image, including cropping and rotating of the image to establish an ROI in the correct orientation, converting the image to grey scale, and establishing a reference length for unit conversion.

2. Initial filtering of the image based on user defined grey scale color thresholds using the global threshold method to identify possible voids from the filaments.

3. Second filtering of the possible voids based on area and aspect ratio to eliminate noise from the possible voids.

4. Final filtering using manual elimination to eliminate all the noise left over in the second filtering.

5. Characteristics of individual voids are extracted using principal component analysis (PCA) and then categorized via hierarchical clustering.

6. Categorized voids are then fitted using the proposed characteristic shapes (triangle, double triangle and tilted hourglass/"merged").

7. With the vertices defined by characteristic shapes fitted to the voids, outlines of each filament can then be traced using vertices from neighbouring voids.

8. At the end, morphological properties of the voids and the filaments are calculated and exported for further analysis.

4.3.2 Pre-processing

Before any analysis steps can take place, stock micrograph will need to undergo a series of pre-processing steps to ensure good accuracy in later steps. Namely, we need to convert the original image from rgb to grey scale, and rotate the micrograph so the rows and columns of the voids are aligned with the edges of the image, as shown in figure 4.6. This is done to simplify the complexity required for future analysis.

A reference scale would also be selected in this step. This is required because all the area threshold values in future steps should be guided by theoretical numbers from printing parameters and will be defined in physical scale (length measurements), whereas the image will be stored in digital scale as data arrays with each entry representing a pixel. For this reason, a reference length should always be included in the micrograph (which is a default setting for most most digital microscope).

At the end, an ROI is selected to identify the region that will be analyzed, romoving unwanted features such as boundaries from the rotated image.

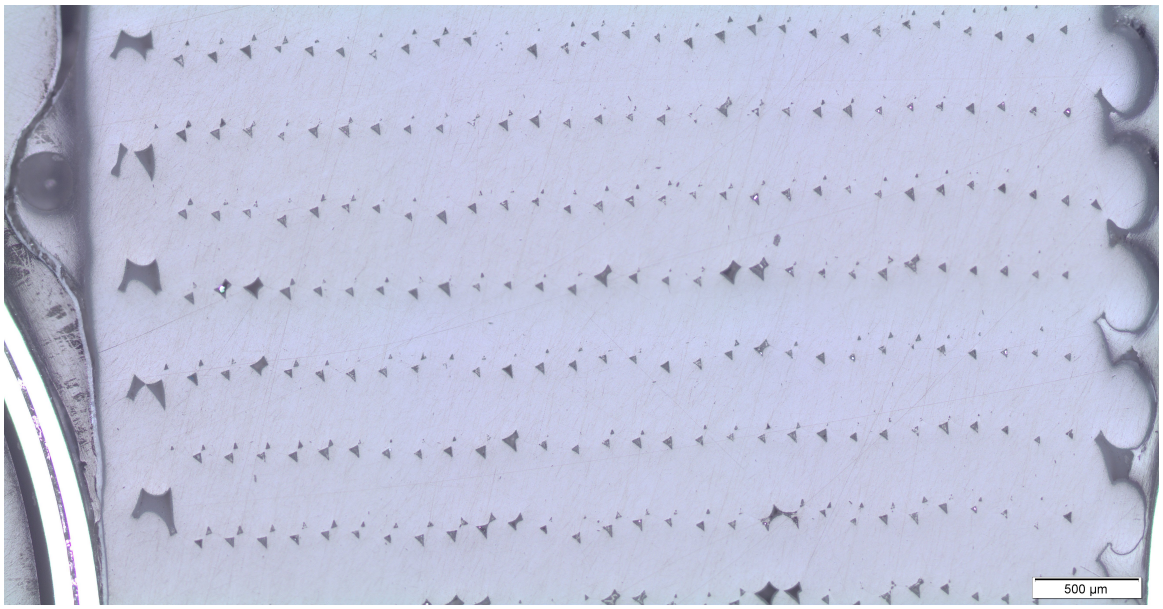

(a) Original micrograph image

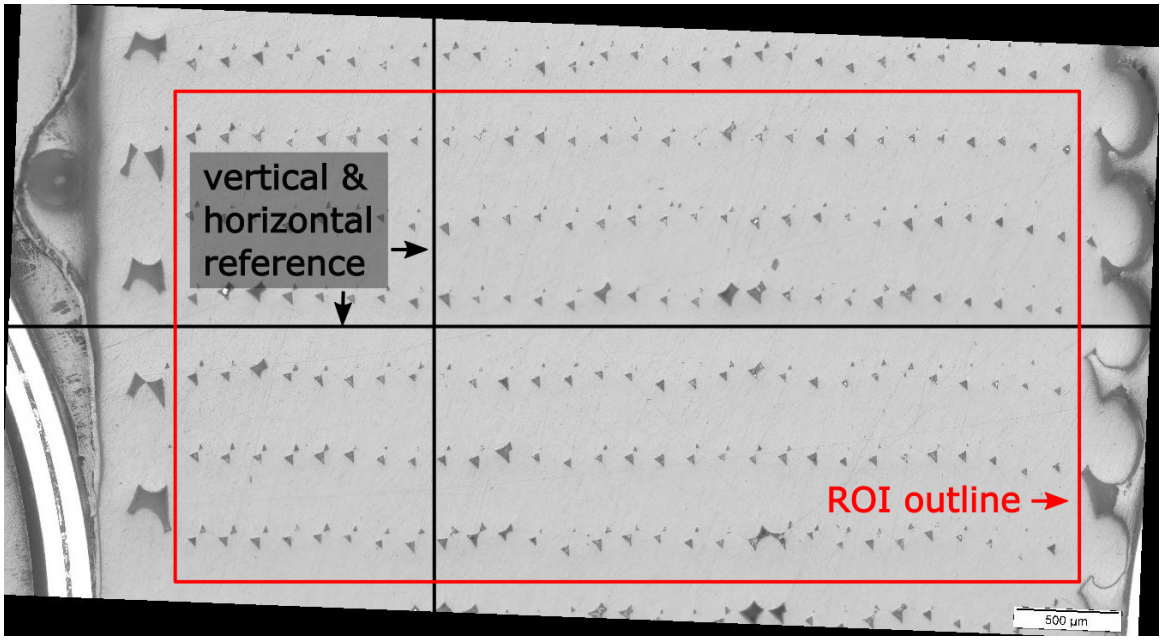

(b) Rotated (& grey scale) image and ROI

Figure 4.6: Comparison between original and rotated micrograph

4.3.3 Filtering

Because voids always show up as a darker color than the rest of the image (filaments), we can use a simple global threshold option to filter out the voids in an efficient manner. To do this, we will first create an array ones the same size as the cropped image (ROI), and set all the pixels that are within the color thresholds to zero. This further simplifies the grey scale image array to a logical array of only ones and zeros. Next, we use a built-in matlab function called *regionprop* to analyze the image, which will identify the zero clusters (voids and some noise) from the array of ones, and store the coordinates of their pixels as vectors [30]. It can also provide us with other information about these clusters, including their areas, aspect ratios, and sizes of their respective rectangular bounding box.

With the pixel lists of all the zero clusters stored, we can perform the second filtering which will separate the voids from noise based on aspect ratio and area thresholds. If a microscopy sample use to generate the micrograph is at least polished to a decent quality, most of the noise clusters will be much much smaller than the voids. On the other hand, scratch marks that are captured by the color thresholds are typically larger than the average noise clusters and are sometimes comparable in their area to some of the smaller voids. Therefore, we need another criteria besides the size to weed out these scratch marks from the actual voids. Fortunately, the nature of scratch marks means that are usually much longer in length than in width, which allows them to be easily filtered out by examining their aspect ratios. However, as some voids, especially those of the "tilted hourglass" shape can sometimes be of a high aspect ratio as well, an upper area threshold is required to stop them from being filtered out. This method is viable because the voids of the "tilted hourglass" shape are going to be larger than the average triangle voids, as by definition, they are formed by the joining of two triangle voids. If a scratch mark is so large that it can bypass this upper area bound, the microscopy sample is clearly badly polished and therefore

does not meet the minimum requirements to be analyzed by our morphology package.

Another aspect that heavily influences the selection of filtering parameters in the current iteration of our code is choosing the balance between noise filtering and detail retention. If we are too aggressive with the filtering, we may inevitably omit too much details of the voids together with the noise. Similarly, we do not want to be too conservative on this step or these can be too much noise left over. In practice, the first and second filtering steps are often run multiple times with different settings to find the optimal ones for the noise-feature balance.

After the second filtering, the remaining zero clusters will be stored as columns in a data array, with their column numbers as their labels. And because we need to preserve as much feature of the voids as possible, we will inevitably have some noise signals left over in our data after the first two filters. The method selected to eliminate these last stubborn noises was manual selection, as it really does not require too much effort if the filtering parameters for the previous two steps were well selected. For the manual elimination step, the zero clusters (voids and noise) are projected onto the original picture with their column numbers next to them, so we can visually see and identify the remaining noise signals (or voids whose shapes are heavily distorted after the filtering). The columns that represent these remaining noises are then eliminated from the data matrix, leaving only voids that can be categorized and characterized later, as visualized in figure 4.7.

Finally, we need to format the filtered data for categorization and shape fitting in the next steps. At this point, we should already have the list of pixels that each voids occupy in vector formats, what we need to do is to frame each voids as individual image arrays of size $h * w$, with the centroid of the voids residing at the center of each individual image. This step is crucial for the next steps where the voids are analyzed and categorized using PCA [31].

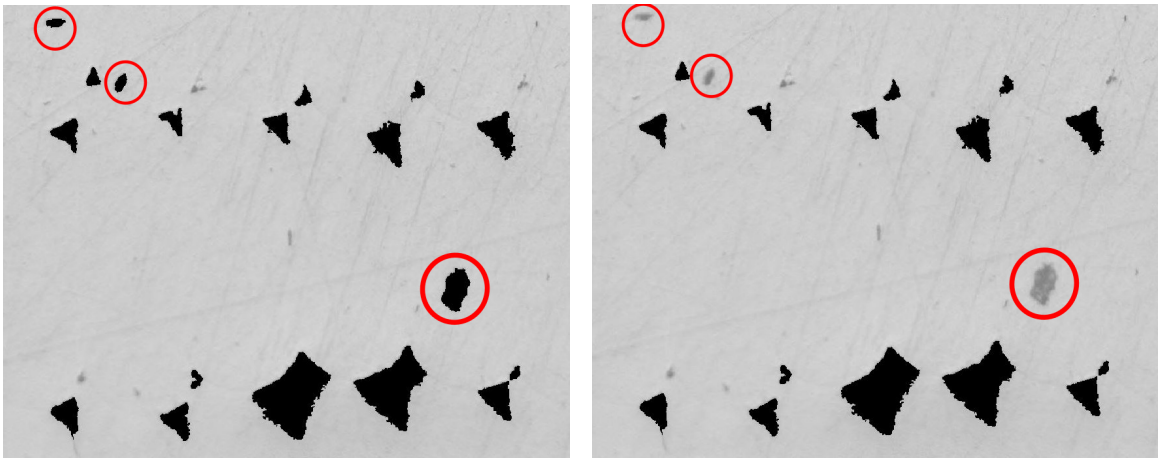

(a) Before manual elimination (b) After manual elimination

Figure 4.7: Before and after manual elimination "filtering"

4.3.4 Void Categorization

Now that we have obtained our nicely conditioned individual void images, we can proceed to analyze them using PCA. Similar to Fourier transform, PCA is a process of expanding a function in some basis representation so that a function $f(x,t)$ over a domain of interest can be represented as shown in equation 4.1, where N is the total number of basis functions, or modes [31]. While PCA is similar to many other decomposition methods such as Fourier transform, the distinct goal of PCA is to find the sequence of orthonormal basis functions $\phi(x)$ so that the first n terms provide the best n-term approximation to the original function $f(x,t)$. These special orthonormal basis functions are called the proper orthogonal modes (POD) for the function f(x,t) [32, 31].

$$f(x,t) = \sum_{j=1}^{N} a_j(t) * \phi_j(x) \tag{4.1}$$

Out of all the decomposition techniques that can be used in PCA, the singular value

decomposition method (SVD) is guaranteed to give the best one, two and three mode approximations of the original function $f(x,t)$ [31]. Given a data matrix A of size $m * n$, SVD decomposes the matrix and represents it as the product of 3 matrices U, Σ, and V as shown in equation 4.2 [31].

$$A = U * \Sigma * V^T \tag{4.2}$$

For analyzing the characteristics of voids, our A matrix will consists of the data representing the voids. Specifically, it should be a data matrix of size $m * n$, where $m = h * w$ is the size of the individual void image arrays in pixels, and n is the total number of voids. Each column of our A matrix represents an individual void image that has been reshaped into a single column vector.

With our A matrix constructed as such, the columns of the $m * n$ matrix U would be the POD modes of individual voids. The diagonal terms of the $n * n$ diagonal matrix Σ would represent the amount of energy carried in the corresponding POD mode. And finally, the columns of the $n * n$ matrix V would contain the information about how much of each POD mode is contained in each data column (pixel list of an individual void image).

The first 3 columns of the V matrix would be what we need to further analyze, as they contain the information about how much of each of the first 3 POD modes is contained in each void, which will allow us to determine the type of each void. The first 3 POD modes were analyzed because SVD is guaranteed to provide the best approximation of the original data as stated before. This also allows us to visualize the data relatively easily in our heads, with each row of V(:, 1:3) representing a point in a 3-D Cartesian space, where the axes represent the levels of the first 3 POD modes contained in the voids.

The analysis method chosen was the ward linkage method. It is a hierarchical clustering algorithm with an existing function in Matlab that also works without supervision (starting points not given) [30]. This method would only require the user to input the

types of void present (triangle vs non-triangle), without the need to select a representative void for each category. And because the clustering is unsupervised, the void clusters that are produced would need to be labeled a posteriori. This is achieved by comparing the average area of the voids contained in one automatically-generated category to the other, again making use of the definition behind the types of void. The category area of the triangle voids would be smaller than that of the non-triangle voids, because the non-triangle voids, whether it be the tilted hourglass or others, by definition, are formed through the joining of two (tilted hourglass or "merged") or more (any other) triangle voids.

After separating the voids into the two main categories of triangle and non-triangle, they are then further separated into one of the final categories:

- Merged, or tilted hourglass, one of the characteristic shapes proposed.
- Triangle pairs or double triangle, one of the characteristic shapes proposed.
- Single triangle, one of the characteristic shapes proposed.
- Any other, which is formed in the rare occasions when two or more sets of voids from the previous categories are joined together.

The "any other" type of voids are distinguished from the "merged" type via a area threshold $n * \overline{A}$, where n is a user-defined constant and $\overline{A}$ is the average area of the overarching "non-triangle" category, as the "any other" voids are going to be larger in area than the "merged" voids by their definition.

The triangle pairs can be identified from the overall "triangle" category via a distance threshold $n * w$, where n is a user-defined constant and w is the smaller of the two line spec settings (layer height or line width). If the closest neighbor of any triangle void is another triangle, and the distance between their centroids are smaller than this threshold, they will then be categorized as a triangle pair. It is also worth pointing out

that if a triangle void is too close to an "any other" type void, it will be categorized as "any other" as well, as it too cannot be used in shape fitting and filament tracing later on.

At the end of the categorization stage, we should have all the information from the filtering stage, plus the category label of each void.

4.3.5 Void Characteristic Shape Fitting

After the voids have been separated into categories, shape fitting can be performed, with the characteristic shapes being fitted to the voids. This helps us in obtaining additional quantifiable measurements of each void, that can be used as a variable in future studies.

It is worth pointing out that the shape fitting algorithm implemented in the current iteration of the morphology package is not the most refined approach, as it bases many of its criteria on geometrical extremes, which in turn is only valid when the micrograph image being analyzed is in the specific orientation that the package is designed for. However, if all the pre-requisites were met (hence the need for pre-processing steps), the current algorithm is able to produce reliable and consistent results.

The triangle shape fitting is relatively straight forward. We first identify the top, bottom, left and right extrema of the void. The top and bottom extrema are taken as the top and bottom vertices of the triangle, and by comparing the length of lines that connect the top and bottom vertices to either the left or the right extrema, we can determine which one should be the third vertex of the triangle (triangle inequality). This works for most of the triangle voids in the image orientation specified in previous steps, as shown in figure 4.8a. However, in special cases such as the one shown in figure 4.8b, top and bottom vertices may not provide the best fit for the given void shape. In this case, areas captured using any 3 out of the 4 extrema are compared, and the combination of vertices that provides the smallest error in area is selected.

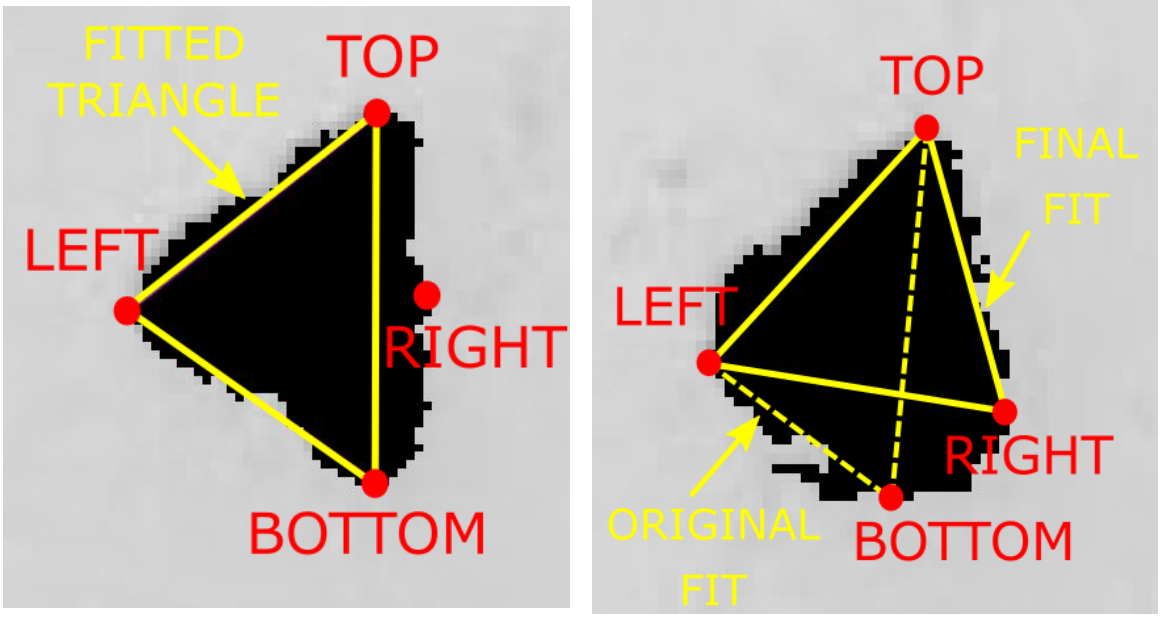

(a) Shape fitting on a well conditioned triangle void

(b) Shape fitting on an ill conditioned triangle void

Figure 4.8: Shape fitting schematics of the triangle void type

The shape fitting for the "merged" type voids is a bit more complicated. As shown in figure 4.9a, the proposed tilted hourglass characteristic shape can be discretized into 6 sides and 6 vertices. Out of the 6 vertices and 6 sides, vertex 1, 3, 4 and 6 are the 4 extrema of the void shape, and side 3 and 6 can be easily determined because of it. To identify vertex 2 and 5, we will need to find the "bend" in the curves connecting vertices 1-3 and 4-6. To numerically implement this, we first calculate the slope of straight lines connecting vertices 1-3 and 4-6. Then, we perform a polynomial fitting of all the perimeter pixel points of the void in question between vertices 1-3 and 4-6. After that, the derivative of the fitted polynomials are calculated, and the point between the two vertices in question where the polynomial derivative equal to the slope of the straight line connecting the two vertices is chosen as vertex 2 or 5.

From this, side 1, 2, 4 and 5 can be easily determined. An example of this process applied on a actual void can be seen in figure 4.9b. Note that the example shown is shown in an adjusted orientation (mirrored and rotated) to make its resemblance to the characteristic shape in figure 4.9a more apparent.

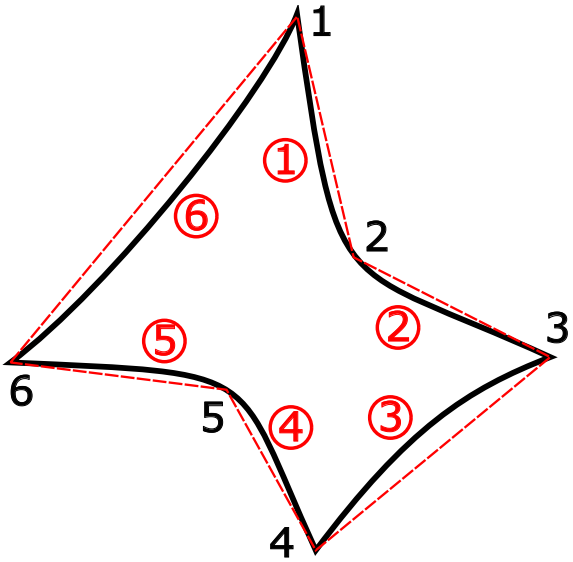

(a) Shape fitting schematic of the "merged" void type

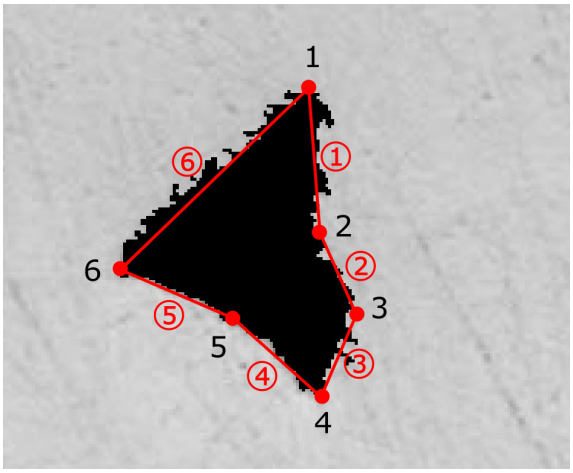

(b) Example of shape fitting on an actual "merged" void

Figure 4.9: Shape fitting schematic and example of the "merged" void type

There are also occasions when shape fitting is not carried out on a void due to it being heavily distorted (if it was not selected during the manual elimination step already). An example is shown in figure 4.10a. As we can see, the upper triangle in this triangle pair has not been well captured in the filtering steps. As a result, the portion of it captured as void is of a highly distorted shape and does not represent the shape of a triangle. We do not want to perform shape fitting on these voids as they can skew our shape fitting data later on. To eliminate these distorted voids from shape fitting, an aspect ratio cutoff was implemented. This was done because most

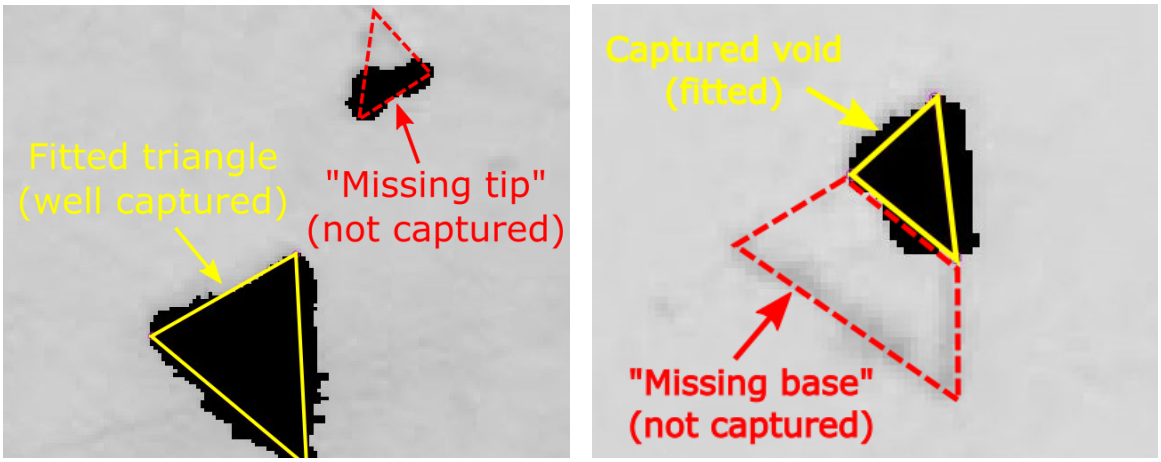

(a) Ill conditioned triangle void that was not shape-fitted ("Missing tip")

(b) Ill conditioned triangle void that was shape-fitted ("Missing base")

Figure 4.10: Examples of badly fitted voids

of these distorted triangle voids are formed by failing to capture one of the corner of a triangle, resulting in a higher aspect ratio compared to the rest of the triangle voids. If it is part of the "base" of a triangle that was not captured (opposite of the previous scenario), the current algorithm will still perform the shape fitting, as the shape of the captured portion of the void would still represent the shape of a triangle (not filtered out due to high aspect ratio), as demonstrated in figure 4.10b. However, this will lead to underestimating the actual void area.

After the shape fitting, the actual "void analysis" part of the morphology code is finished. We now have all the individual voids with characteristic shapes fitted to them with defined vertices, as well as their area and locations within the micrograph ROI.

4.3.6 Filament Perimeter Tracing

The last step of the morphology analysis is to produce the outline of filaments from the void analysis results. The boundary of each filament is identified by the voids at its four corners. However, as there can be different types of voids at any of the four corners of a filament, which vertices to use from a given void is entirely determined by which corner of the filament it occupies (in the pre-determined orientation).

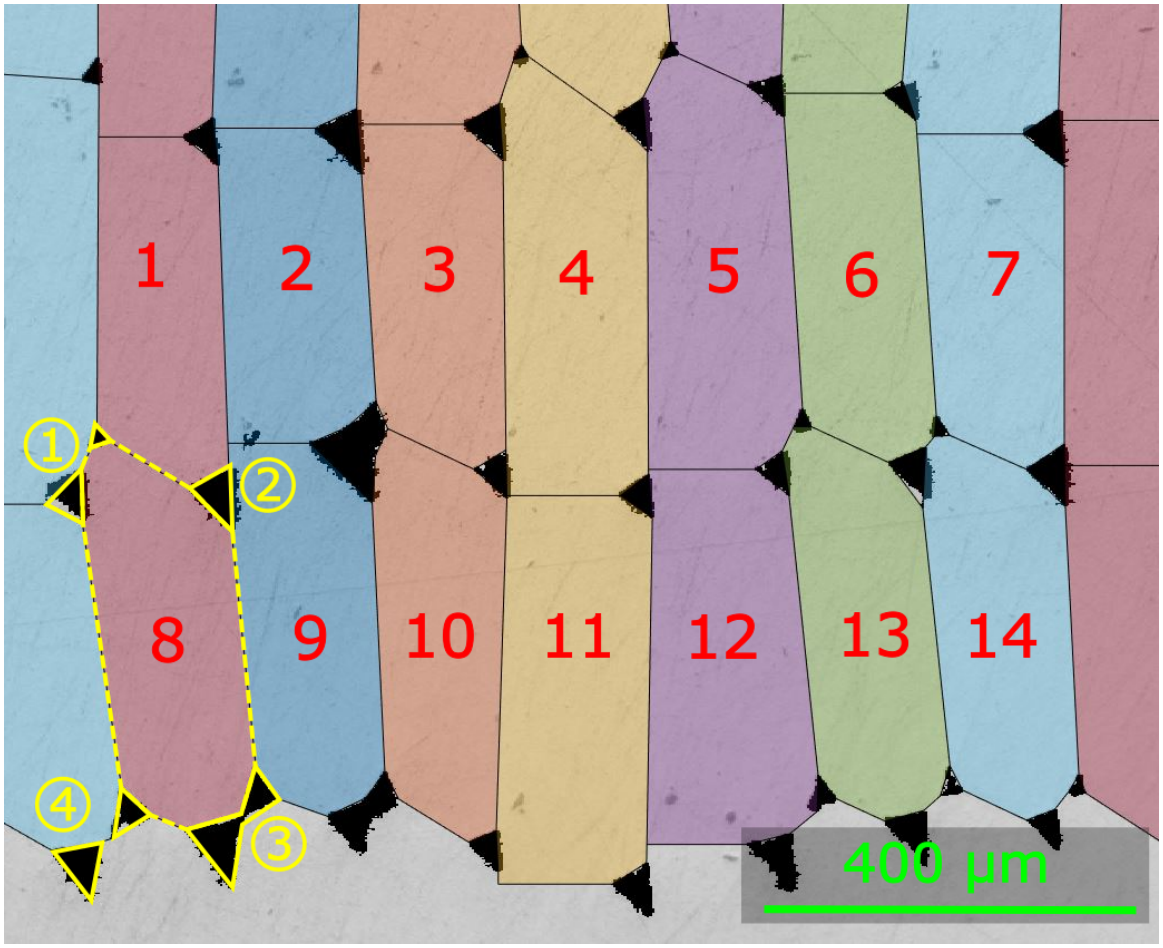

Figure 4.11: Traced filaments

Figure 4.11 shows a collection of different scenarios in filament tracing. Let's label the corners of each filament from 1 to 4 starting from the top left corner, as demonstrated

in figure 4.11 on filament number 8. If we look at filament number 8 and filament number 13, we can see that their perimeter vertices are entirely defined by vertices of the four voids at their corners. This is because the voids at each corner all have at least 2 vertices that "wraps around" that corner. For example, in filament 8, void 2 is fitted as a triangle void (misidentified because the smaller triangle of the pair was filtered out) that has one vertex pointing down and one pointing left, "wrapping around" the top-right corner of filament number 8. Similarly, void 3 of filament 8, a merged type, has 3 vertices that wraps around the bottom-right corner of filament 8. This scenario is the simplest as all the vertices needed to complete the perimeter of the filament have been identified in previous steps.

However, if we take a look at filament number 1, 2 and 12, we can see that not all of their perimeter vertices are vertices from the voids. For example, void 1 of filament 2, a triangle type, only has one of its vertices pointing down, but none that points to the right. Therefore, the top side of filament 2 (if we imagine the filaments as approximately quadrilaterals with top, bottom, left and right sides) is entirely determined by void 2. In such scenarios, we produce a horizontal line that starts from the left vertex of void 2, and intersects void 1 at one of its sides. This intersection point will now serve as the right vertex of void 1, and defines the top-left corner of filament 2 along with the bottom vertex of void 1. The top side of filament 1 is similar to that of filament 2. But unlike filament 2, we can see that the horizontal line from void 2 does not meet any side of void 1, as they are misaligned in the vertical direction. In this case, the intersection is defined as that between the horizontal line from void 2 and the left side of the filament, which would need to be defined a priori. For this reason, the algorithm traces the left and right sides of all the filaments, which are always identified by the top or bottom vertex of the voids, before tracing the top and bottom sides of the filaments, which can contain part of the perimeters from the voids.

This is the end of the morphology analysis package. At this point, we have obtained

the shapes of all the voids and filaments (that can be identified and fitted/traced). The statistical analysis of the data obtained will be discussed in the next chapter.

Chapter 5

EXPERIMENTAL RESULTS

5.1 Uni-Axial Tension Test Results

As previously noted in chapter 2, the extruder assembly on our 3-D printer was changed half way through the project. Although our original uni-axial tests were completed before the extruder change, we still re-ran the uni-axial tests with specimens manufactured using the new extruder as the SENB tests were still pending at the time, and we wanted to ensure the consistency in material performance between tensile and SENB tests. A comparison of the void morphology before and after the extruder change is shown in figure 5.1

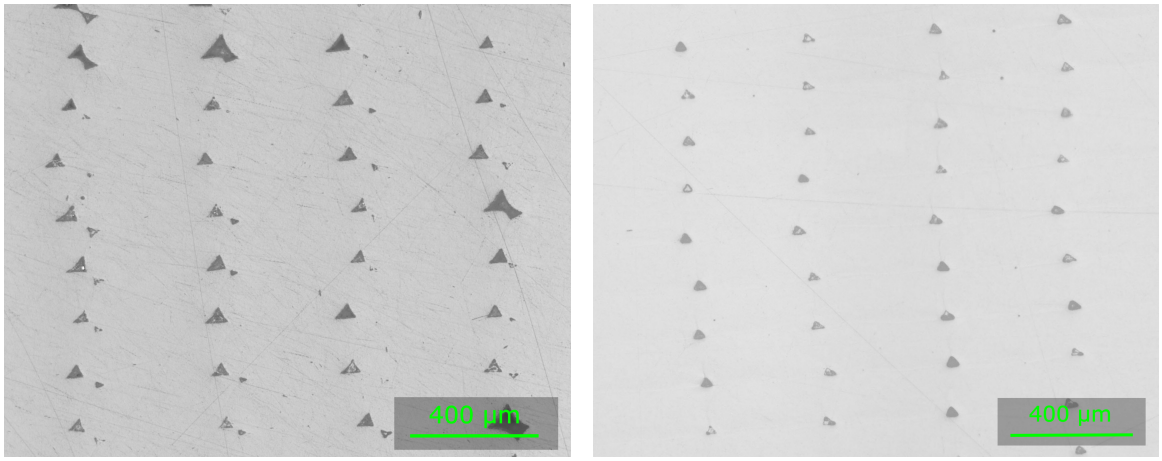

(a) Voids before extruder change (b) Voids after extruder change

Figure 5.1: Comparison of void shapes before and after extruder change

The stress-strain curves from the initial tests (before extruder change) are shown in

figure 5.2, and the calculated material properties are summarized in table 5.1. Four samples of each layup were printed for the initial tests.

The stress-strain curves from the more recent tests (after extruder change) are shown in figure 5.3, and the calculated material properties are summarized in table 5.2. Six samples of each layup were printed for the new tests.

By comparing the mechanical properties of the new and old material, we can observe a decrease in Young's moduli and an increase in strengths in the printed material following the extruder change. The increase in strength was likely a result from the reduction in void fraction in the material (I will further discuss in the morphology section of this chapter), but it was unclear what might have caused the drop in Young's moduli.

My hypothesis for reason behind the drop in Young's moduli was the possible change in printing temperatures. Although all the printer settings were kept the same, the actual nozzle temperature during printing could have been different before and after the extruder change. This was possibly the result of a faulty nozzle temperature sensor in the old extruder assembly. As we have seen with the bed temperature sensor, the suspicion of a malfunctioning temperature sensor is definitely not an unfounded claim. Although we may never know whether the old sensor was actually faulty, as it was destroyed during the system malfunction, we can still test the hypothesis on the effect of changing printing temperatures by printing and testing samples manufactured using different temperature settings. Unfortunately, due to the time constraint of this thesis, this study would have to be done in future projects.

We can see from both figure 5.2 and 5.3 that the 0°and the 90°samples do not experience significant softening before peak stress, and they all fracture in a brittle manner after the peak stress was reached. The +-45°samples were the only ones that exhibited significant non-linear behavior post-peak before fracture.

The new +-45°test results have depicted a much high degree of post-peak plasticity compared to the old results, with visually significant plastic deformation such as

Property	Average value	Standard Deviation	Unit
E_1	3789.1	116.228	MPa
E_2	3390.6	107.904	MPa
G_{12}	1298.5	43.1326	MPa
ν_{12}	0.3528	0.0059	
ν_{21}	0.2917	0.0070	
S_{1y}	49.9326	1.3769	MPa
S_{2y}	24.8921	1.4859	MPa
S_{12y}	17.0706	1.0729	MPa
S_{1u}	55.4812	0.8628	MPa
S_{2u}	24.9354	1.5137	MPa
S_{12u}	21.5451	0.8853	MPa
ϵ_{1y}	0.0159	0.3988E-03	
ϵ_{2y}	0.0096	0.7049E-03	
γ_{12y}	0.0159	0.9699E-03	
ϵ_{1u}	0.0184	0.2624E-03	
ϵ_{2u}	0.0096	0.7443E-03	
γ_{12u}	0.0257	1.700E-03	

Table 5.1: Calculated mechanical properties (old)

Property	Average value	Standard Deviation	Unit
E_1	3397.2	66.0917	MPa
E_2	2872.1	71.9763	MPa
G_{12}	1106.1	12.8842	MPa
ν_{12}	0.3812	0.0187	
ν_{21}	0.3378	0.0102	
S_{1y}	57.0405	1.9610	MPa
S_{2y}	30.3986	2.6744	MPa
S_{12y}	21.0501	0.8498	MPa
S_{1u}	57.5475	2.2686	MPa
S_{2u}	30.3986	2.6744	MPa
S_{12u}	24.0669	0.6382	MPa
ϵ_{1y}	0.0191	0.8379E-03	
ϵ_{2y}	0.0112	1.0682E-03	
γ_{12y}	0.0218	0.7991E-03	
ϵ_{1u}	0.0195	1.1589E-03	
ϵ_{2u}	0.0112	1.0682E-03	
γ_{12u}	0.0318	0.7247E-03	

Table 5.2: Calculated mechanical properties (new)

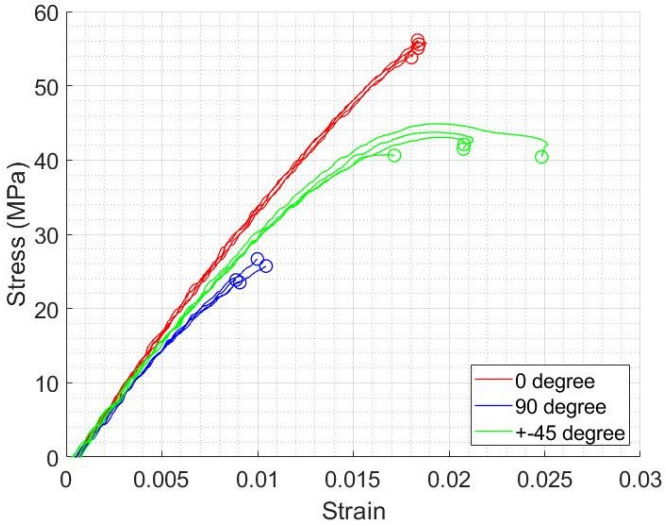

Figure 5.2: Uni-axial stress-strain curves (old, remote strain)

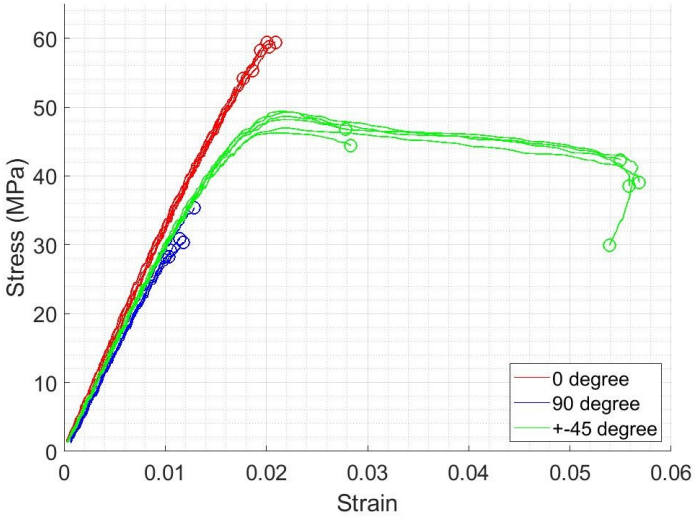

Figure 5.3: Uni-axial stress-strain curves (new, remote strain)

necking observed during testing on some samples and accompanied by visually distinguishable initial crack formation and development. An example is shown in figure

5.4. This prompted further study into the localized plasticity before failure in the new samples. Strain values were selected at the locations of stress concentration. The stress-strain curves obtained from this method is shown in figure 5.5.

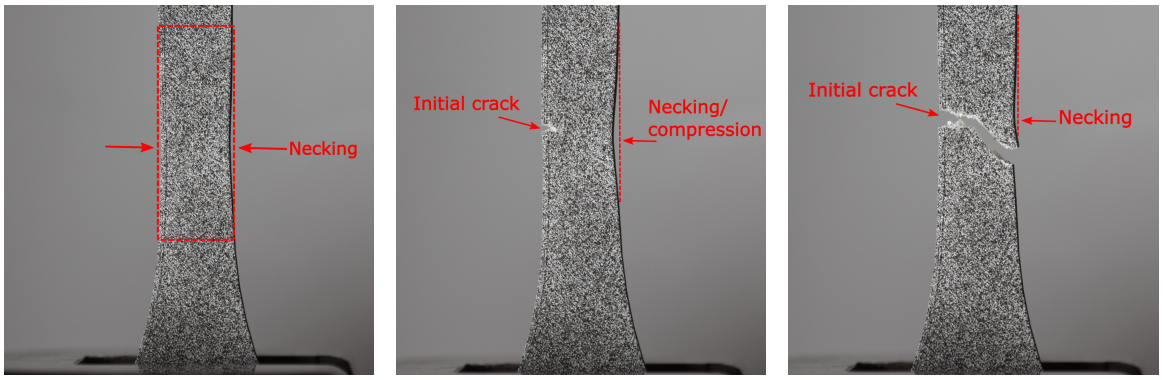

(a) Necking before initial crack formation

(b) Formation of initial crack and more plastic deformation

(c) Residual plastic deformation post-fracture

Figure 5.4: Example of plastic behavior in +-45 °tensile specimens

Comparing the stress-strain curve at and away from stress concentration shows us that although the overall structure may break almost brittlely, we can still see local structure exhibit post-peak plastic behaviors.

This phenomenon is less pronounce in the 90°samples. I suspect this is because the print direction aligns the weaker filament interfaces perpendicularly to the load direction, allowing any crack to propagate quickly before any local structure can plastically deform significantly.

We can see more pronounced localization in the 0°samples. As the filaments are aligned with the loading direction, the structure is made stronger, and with less change to develop a transverse crack, allowing local plastic deformation to take place. It is worth pointing out that the localization in all the 0°samples take place at the point where the gauge area transitions to the tab. This is exactly what was expected,

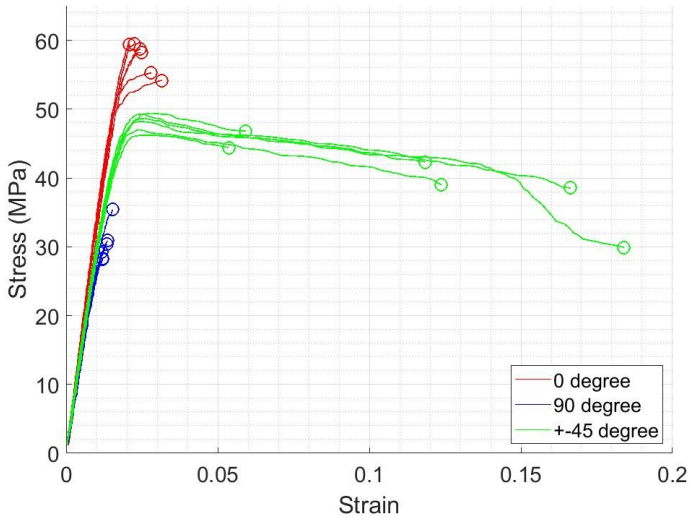

Figure 5.5: Uni-axial stress-strain curves (new, local strain)

as it is coincident with the stress concentration introduced by the fillets in the dog bone specimen design.

Post-peak plasticity is the most pronounced in +-45°samples. The alternating print direction in the layup results in the alternating of voids and defects as well. This in turn acts as a barrier that inhibits any crack that may form at one of the stress concentration from propagating through the thickness of the specimen, allowing local structure at stress-concentrations to dissipate energy by deforming plastically and via a series of local fracture mechanisms such as delamination, filament pullout, etc.

5.2 Single Edge Notched Bending (SENB) Test Results

The load-displacement curves from the SENB tests are shown in figure 5.8. To avoid the outlier effect, we removed the samples that displayed a drastically different fracture behavior than the rest of the specimens of the same size and print direction. Specimen 1 from the 0°/36mm samples, specimen 3 from the +-45°/72mm samples, specimen 5 from the 90°/36mm samples and specimen 5 from the 90°/72mm samples

were determined as outliers. Since we tested six samples for each layup/size configuration, we believe the remaining data from each data set were still representative of the actual material behavior.

The area under the load-displacement curves were calculated using the trapezoidal integral method with the *trapz* function in Matlab [30].

The actual width and height of each specimen were measured before the test. Length of the crack (from the mouth of the notch to the tip of the razor generated pre-crack) in each specimen was measured after the test.

The crack lengths were measured a posteriori because it is very difficult to determine the crack tip location from the surface of the specimens before the test. In contrast, the location of the crack tip can be easily determined from the cross section of the specimens after the test when the cross section is exposed via fracture. This is because the initial crack surface can be easily distinguished from the fracture surface induced during the test based on their visual appearances. With these measurements, we can calculate the area in front of the crack tip A_c in each specimen.

With the areas under the load-displacement curves and the areas in front of the crack tips, we then calculate the fracture energy of each specimen using equation 3.3.

As stated in chapter 3, these fracture energy values may not accurately reflect the actual material property, because our specimens could not be broken entirely. To try compensate for this possible error introduced by hardware limitations, fracture energy values from the "extended" load-displacement curves were calculated. The results are listed in table 5.3 and visualized in figure 5.6.

The extended load-displacement curves were generated by adding linear extensions to the end of existing load-displacement curves. The slope of each linear extension was calculated from the last 10% of the respective load-displacement curve. The load-displacement curves were extended until the load reaches 0.

However, although this curve extension method works well with load-displacement curves that are still not completely "flattened" towards the end of the curve (the

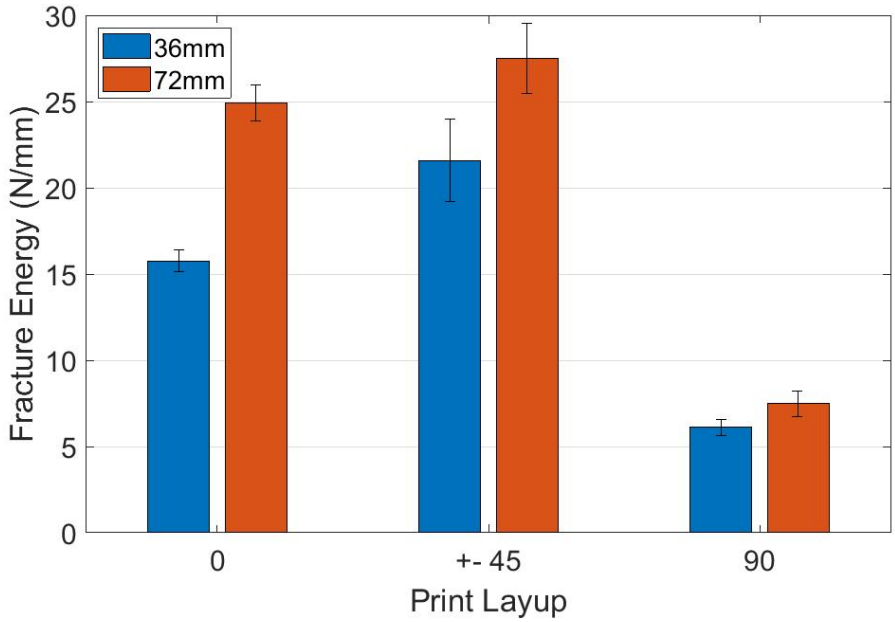

Figure 5.6: Distribution of fracture energy

0°and +-45°samples), it does not work particularly well on the curves where the load has completely converged (the 90°samples). Therefore, a uniform extension was performed on the 90°samples instead, where we simply extend the 90°load-displacement curves horizontally until they reach a desired final displacement value. The target final displacement values used for the 90°extensions were the average projected final displacement values from 0°and +-45°samples. The calculated projected errors are tabulated in table 5.4. Examples of the extended load-displacement curves can be seen in figure 5.7.

Overall, most of the projected errors are very small, meaning that the vast majority of the fracture energy can still be captured form our tests even though the samples cannot reach complete failure. This is because the final loads on most samples are much lower than their respective peak loads, as can be seen in figure 5.8.

The only exceptions are the +-45°/36mm samples, where most of the projected errors

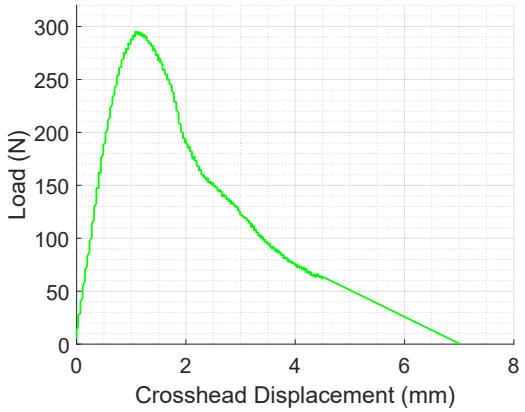

(a) Extended load displacement curve (36mm +-45°)

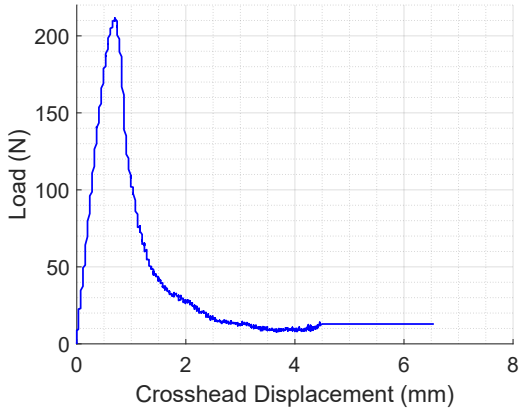

(b) Extended load displacement curve (36mm 90°)

Figure 5.7: Extended/Interpolated load-displacement curves examples

are above 10%. This may have been the effect of the high final loads to peak loads ratio as shown in figure 5.8, which allows the "projected tail region" of their load-displacement curves to capture much more energy than that in other samples.

As for the fracture energy values, we can see from figure 5.6 that the fracture energy of the 72mm samples are larger than that of the 36mm samples for both the 0°and +-45°layups. This could be a result of the plasticity in these samples, where the Fracture Process Zone (FPZ) and the Plastic Zone (PZ) area able to develop more fully in the larger samples than in the smaller ones, resulting in the difference in the measured fracture energy. This size effect is a well known phenomenon occurring in quasibrittle materials, i.e. materials in which the size of the largest heterogeneity is not negligible compared to the structure size [33]. Examples of quasibrittle materials include concrete [33], fiber composites [34, 35, 36, 37], textile composites [38, 39, 40, 41, 42, 43], discontinuous fiber composites [44, 45], polymer nanocomposites [46, 47, 19, 48, 49, 50, 51, 52, 53, 54, 55], and rocks [56, 57].

In contrast, the fracture energy of the 72mm samples and that of the 36mm samples are about the same for the 90°layup. This was likely caused by the void orientation in the 90°samples. With the voids and the weaker interface between filaments being aligned parallel to the initial crack, the crack can propage through these weak points more easily than it can in samples with the other layups. This can result in less plasticity, which allows the FPZ and PZ to fully develop even in the smaller samples, and therefore produce similar fracture energy levels across the 36mm and the 72mm samples.

5.3 Cross-Section Morphology Study Results

For the morphology study, microscopy samples of 0°samples were prepared using the procedure described in chapter 4. The study was conducted on samples from both before and after the extruder change. Table 5.5 shows a summary of the results from the morphology study. The micrographs that were analyzed to obtain these results can be found in appendix.

As we can see from table 5.5, changing the nozzle has had a significant impact on the types of void present in our printed material. The voids in our material after the extruder change are predominantly the single triangle type (entirely in the sample analyzed in table 5.5) that are similar to the results from previous literatures [28, 10, 3], while the majority of the voids in our material before the extruder change were instead made up of the more obscure tilted hourglass and its double triangle variant. However, it was lucky for us that we encountered the obscure void types first, so our morphology analysis package could be designed to deal with them.

We can also see a significant drop in the mean void area after the extruder change with a decrease of 34%, while the mean filament area stayed relatively unchanged, with a increase of only 3.4%. Consequently, the void fraction reduced significantly following the extruder change, with a drop of 36%.

Please note that the number of voids are calculated based on the total number of

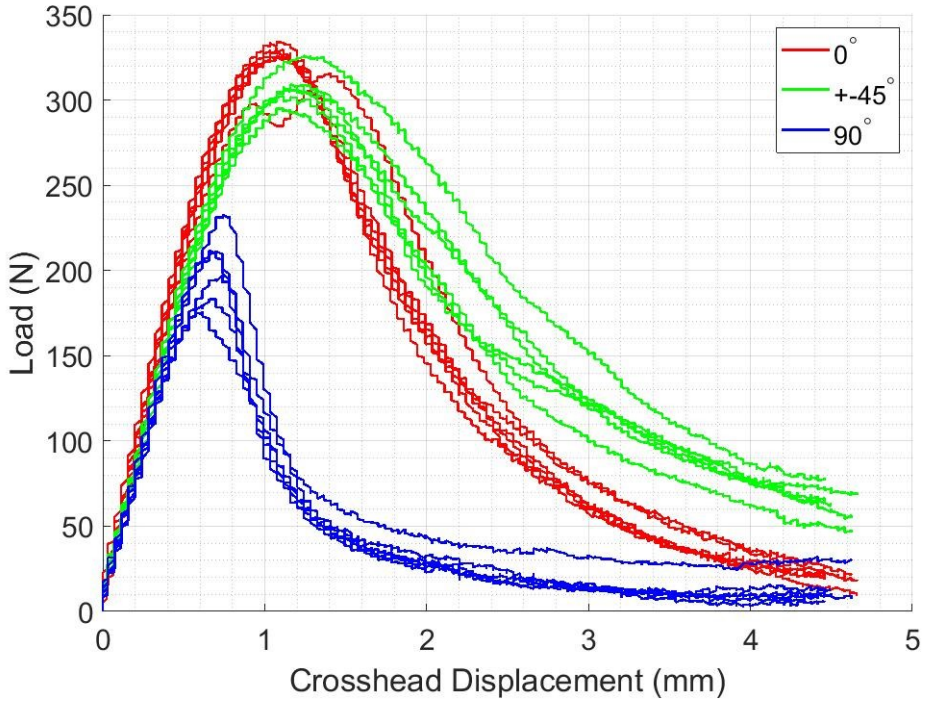

(a) Load-displacement curves of the 36mm SENB samples

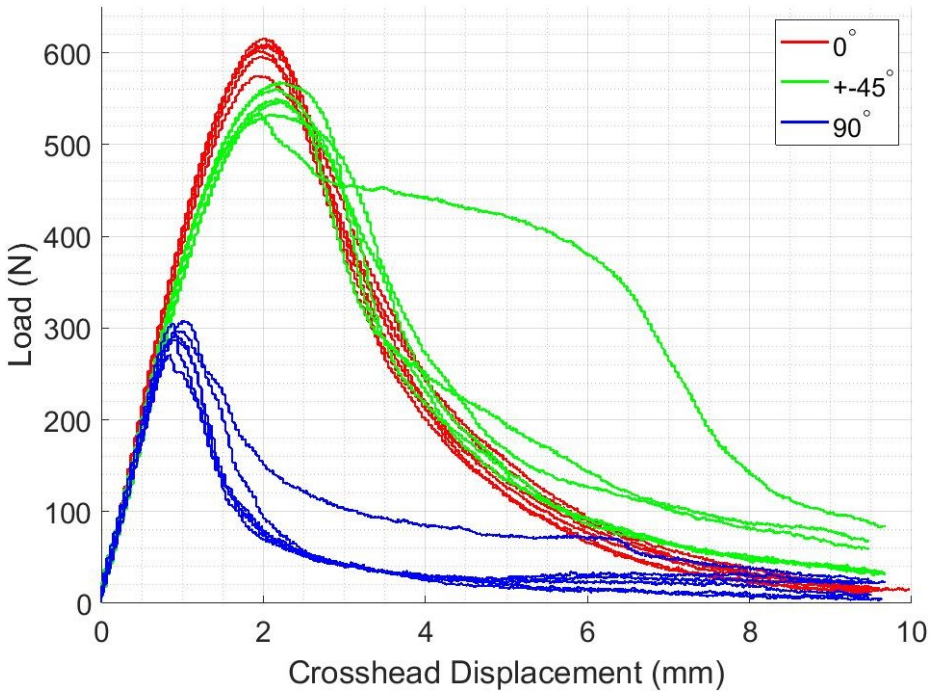

(b) Load-displacement curves of the 72mm SENB samples

Figure 5.8: Load-displacement curves of SENB samples

Specimen number / Layup	Fracture energy (N/mm) / Specimen size	Fracture energy (N/mm) / Specimen size
0°	L = 36mm	L = 72mm
1	N/A	26.19
2	16.49	25.99
3	14.88	25.22
4	16.16	24.18
5	15.70	23.58
6	15.56	24.32
Average	15.76	24.91
+-45°	L = 36mm	L = 72mm
1	20.03	25.70
2	20.34	29.54
3	20.37	N/A
4	24.66	26.00
5	19.47	26.44
6	24.63	29.85
Average	21.58	27.50
90°	L = 36mm	L = 72mm
1	5.927	6.422
2	6.092	7.323
3	5.994	8.230
4	6.909	7.246
5	N/A	N/A
6	5.612	8.192
Average	6.107	7.483

Table 5.3: Fracture energy of SENB specimens

Specimen number / Layup	Projected fracture E error (%) / Specimen size	Projected fracture E error (%) / Specimen size
0°	L = 36mm	L = 72mm
1	N/A	0.8592
2	1.473	0.5666
3	0.4025	0.6259
4	2.221	0.6263
5	2.263	0.4458
6	1.434	0.6974
Average	1.559	0.6369
+-45°	L = 36mm	L = 72mm
1	5.256	1.926
2	9.710	4.237
3	10.12	N/A
4	19.98	3.874
5	8.573	2.677
6	15.16	5.438
Average	11.47	3.630
90°	L = 36mm	L = 72mm
1	8.060	2.076
2	10.87	3.298
3	7.640	9.130
4	9.533	4.525
5	N/A	N/A
6	5.786	9.648
Average	8.377	5.736

Table 5.4: Projected error in fracture energy

	Before extruder change	After extruder change
Total number of voids identified	260	174
Total number of voids fitted	251	170
Number of fitted triangle voids	74	170
Number of fitted triangle pairs	81	0
Number of fitted merged voids	15	0
Actual number of filaments in sample	140	154
Filaments traced	133	120
Mean void area (mm^2)	$1.654 * 10^{-3}$	$1.089 * 10^{-3}$
Mean filament area (mm^2)	$57.36 * 10^{-3}$	$59.34 * 10^{-3}$
Void fraction	2.883%	1.835%

Table 5.5: Morphology results overview

pixel clusters from the micrograph that were identified as voids. Namely, the two triangles in a triangle pair were counted separately. However, the void area of a triangle pair is calculated as the area sum of the two triangles within the pair. While the number of voids that are identified as well the the number that are shape-fitted are both indicators of how well the filtering was carried out and how well the microscopy samples were prepared, the area of each individual or set of voids are morphological characteristics as a resultant of given printing parameters. Therefore, it makes sense to count the two pixel clusters in a triangle pair separately, but to calculate their areas together as a single morphological unit.

To further analyze the morphological characteristics, statistical studies were conducted on the void area (A_v), filament area (A_f) and filament inertia (I_{f1}, I_{f2}). We calculated their mean, standard deviation, skewness and kurtosis. Based on these results, we then determined the statistical distribution within each morphological

measurement. The results are summarized in table 5.6.

To avoid the effect of outliers on the entire data set, they were eliminated before all the statistical calculations took place. In this case, outliers are defined as any data point that are beyond 3 standard deviations away from the mean, where both the standard deviation and the mean are preliminary results calculated from the original data set with outliers.

To determine whether each data set follows the standard normal (Gaussian) distribution, the skewness and the kurtosis of the data sets were also calculated. The skewness is a measurement of the location of the median and the mode of a given data set relative to that of the mean, and can be used to determine whether non-symmetric distribution functions are needed to achieve a good fitting. The kurtosis is the measurement of how "sharp" the peak of a given distribution is relative to the standard normal distribution, which has a kurtosis of zero. The allowable skewness and kurtosis are both properties that are independent from the distribution of the data sets, but are instead determined by the size of them. Therefore, the allowable skewness and kurtosis are the same for A_f and I_{fi}, as they have the same sample size (number of filament traced). Although skewness and kurtosis are good general indicators of whether a certain data set follows the normal distribution, we will later see that it does not always work.

We can see from table 5.6, that the extruder change had not only resulted in the drop in void fraction of the material, but in the consistency of the extruded filament as well, as evident by the reduction in standard deviations of morphological measurements across the board. This supports the claim made earlier in chapter 2 based on visual inspection, which stated that the new material was of superior print quality.

To better determine the type of distribution exhibited by each data set, Lilliefors tests [58] were conducted on each set of morphological measurement, testing whether the data set follows normal, lognormal, or Weibull distribution [59]. Both the lognormal and the Weibull distributions are non-symmetrical, allowing us to better account for

the skewness exhibited in some of the data sets. We would also like to test distribution types that allows us to account for pointier peaks in our data sets, such as logistic and log-logistic distributions. However, they are not supported by the Lilliefors test algorithm in Matlab [30].

In order to test the logistic and log-logistic distributions, we decided to quantitatively compare the goodness of fit of one of the distributions that have passed the Lilliefors test to the goodness of fit of a proposed distribution that needs to be tested. If the goodness to fit of the proposed distribution is deemed better than that of a distribution which has passed the Lilliefors test, we can then safely conclude that the proposed distribution is also a viable, and potentially better fit for a given set of data.

To implement this approach, the *Distribution Fitter App* in Matlab was used. It allows us to fit different distribution curves to a given set of data, and is able to export the cumulative distribution function (CDF) of the fitted curve. The CDF of the fitted curve is then compared to the empirical CDF of the data set on which the curve was fitted. The goodness of fit value can be calculated using the chi-squared test, shown in equation 5.1, where O_i is the observed value (empirical CDF) and E_i is the expected value (fitted CDF). By comparing the χ^2 values of each type of fitted distribution, we can determine the best type of distribution for describing our morphological measurements.

$$\chi^2 = \sum \frac{(O_i - E_i)^2}{E_i} \tag{5.1}$$

A summary of the best type of distribution as well as all the viable distributions (ones that passed the Lilliefors test) for each morphological measurement is listed in table 5.7. Figure 5.9a shows the histogram of I_{f2} of the new material, with a log-normal distribution curve. Please note that instead of showing the frequency of data in each bin, the histogram in figure 5.9a is normalized to the probability density function of the data set. Figure 5.9b shows the comparison between the empirical CDF of I_{f2} and the CDF of the fitted log-normal distribution curve. This is a visual representation

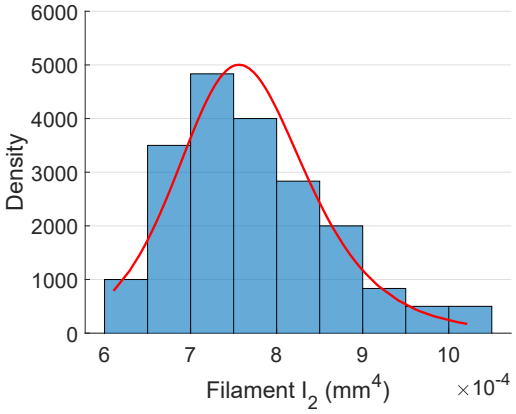

(a) Density histogram with fitted log-logistic distribution curve

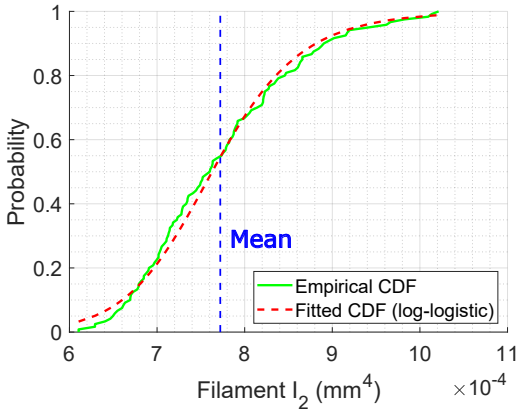

(b) Comparison between empirical CDF and fitted CDF

Figure 5.9: Statistical figures of filament I_2 (after extruder change)

of the goodness of fit of the selected type of distribution The figure 5.9 equivalent for all the other measurements can be found in appendix.

Before extruder change				
	Mean	Standard deviation	Skewness	Kurtosis
A_v (mm^2)	$1.654 * 10^{-3}$	$7.508 * 10^{-4}$	1.4647	2.8922
A_f (mm^2)	$57.36 * 10^{-3}$	$5.339 * 10^{-3}$	0.2921	-0.0951
I_{f1} (mm^4)	$1.040 * 10^{-4}$	$2.093 * 10^{-5}$	0.5058	0.1547
I_{f2} (mm^4)	$7.205 * 10^{-4}$	$1.480 * 10^{-4}$	0.6413	0.1827
Allowable skewness & kurtosis for A_v			±0.3757	±0.7472
Allowable skewness & kurtosis for A_f and I_{fi}			±0.4217	±0.8373

(a)

After extruder change				
	Mean	Standard deviation	Skewness	Kurtosis
A_v (mm^2)	$1.089*10^{-3}$	$3.384*10^{-4}$	0.1234	-0.1251
A_f (mm^2)	$59.34*10^{-3}$	$2.739*10^{-3}$	0.1159	-0.4649
I_{f1} (mm^4)	$1.110*10^{-4}$	$1.073*10^{-5}$	0.2677	0.0344
I_{f2} (mm^4)	$7.722*10^{-4}$	$9.022*10^{-5}$	0.6793	0.0181
Allowable skewness & kurtosis for A_v			±0.3725	±0.7408
Allowable skewness & kurtosis for A_f and I_{fi}			±0.4418	±0.8767

(b)

Table 5.6: Detailed morphology results

Morphological measurement	Best distribution	Other viable distributions
A_v (old)	Log-logistic	Log-normal
A_f (old)	Log-logistic	Normal, Log-normal
I_{f1} (old)	Log-logistic	Log-normal
I_{f2} (old)	Log-logistic	Log-normal
A_v (new)	Normal	Weibul
A_f (new)	Log-normal	Normal
I_{f1} (new)	Log-logistic	Log-normal
I_{f2} (new)	Log-logistic	Normal, Log-normal

Table 5.7: Morphological measurements and their best distribution fit

Chapter 6

DISCRETE FINITE ELEMENT MODELLING

6.1 Discrete Finite Element Model Overview

There are many scholars who have attempted modeling additively manufactured materials (specifically fused deposition modeling) using the finite element method with a homogenized approach [15, 28, 14, 60, 61]. In this method, the mesostrucre of the FDM 3D printed material is broken down into small units called Repeating Volume Elements (RVE), which was used to determine the effective constitutive matrix of the 3D printed material [15]. This process of determining the properties of a material from the properties of its constituents is called homogenization. Although this method is able to capture the elastic response of a FDM 3D printed structure, it is not able to predict and model its fracture and failure mechanics [15, 61].

Therefore, we chose to use the discrete FEM model developed by Antonio Deleo from MAMS lab for this project. The model is called *A Fast and Efficient Discrete Model for Composites*, or "FastDM4C" for short. As the name suggests, the FastDM4C model was originally proposed as a way to model fracture in laminate composite materials. However, as our FDM 3D printed material is also anisotropic in nature and has many common characteristics as laminate composites, we think the model would work for modeling FDM 3D printed material as well.

In the FastDM4C model, a laminate structure is decomposed into single plies, and each ply or lamina decomposed into arrays of rectangular unit cells that are aligned with the direction of the lamina [62]. The unit cells are composed by either truss or beam elements as shown in figure 6.1 [62]. For a multi-layer laminate, the interaction between each neighboring lamina is modeled by inter-laminar beams as shown in

figure 6.2 [62].

While the lattice members behave as isotropic materials, their connection and kinematic constraints allow the model to behave macroscopically as a anisotropic material [62]. And because the fiber and matrix are modeled explicitly, all the damage mode and mechanisms can be captured [62].

To capture damage, the mechanical behaviors of elements in the discrete model follows a modified Hooke's law (equation 6.1) that is either based on the Linear Traction-Separation Law (equation 6.2) or the Bi-Linear Traction-Separation Law (equation 6.3) [63, 62].

$$\sigma = (1 - D_i)E\epsilon \tag{6.1}$$

$$D_i = \frac{\epsilon_f(\epsilon - \epsilon_{elastic})}{\epsilon(\epsilon - \epsilon_{elastic})} \quad for \quad \epsilon > \epsilon_{elastic} \tag{6.2}$$

$$\begin{aligned} D_i^1(\epsilon) &= 1 - \frac{(\epsilon - \frac{f_t}{E})s_1(\epsilon) + f_t}{E\epsilon} \quad for \quad \epsilon_{elastic} < \epsilon < \epsilon_k \\ D_i^2(\epsilon) &= 1 - \frac{(\epsilon - \epsilon_k)s_2(\epsilon) + f_t}{E\epsilon} \quad for \quad \epsilon_k < \epsilon < \epsilon_f \end{aligned} \tag{6.3}$$

Because we are modeling a single material system in this project, the "fiber" and "matrix" elements in the model do not represent the actual fiber and matrix as they would in a composite material. However, each of them can still be related to features in a FDM 3D printed material. The fiber elements in this case represent the extruded filaments in a 3D printed material. The matrix and diagonal elements represent the connection and interaction between each extruded filaments in the same layer, and the inter-laminar beams represent the connection between neighboring layers in a 3D printed material.

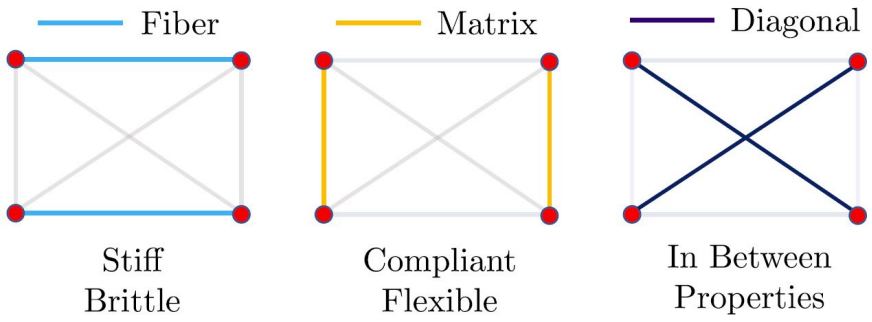

Figure 6.1: Unit cell configuration in the FastDM4C model

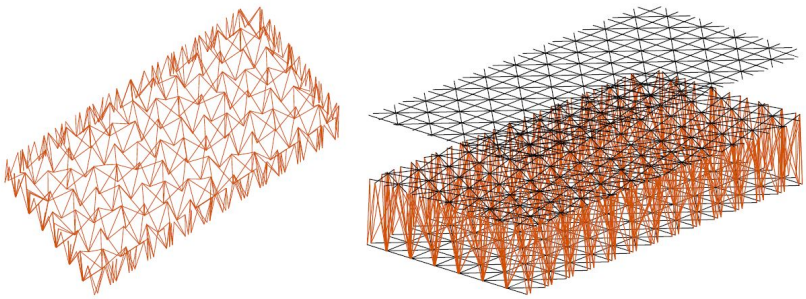

Figure 6.2: Inter-laminar beams configuration in the FastDM4C model

6.2 Model Calibration Methodology

To generate the discrete model, a Matlab script provided by Mr. Deleo was used to create an ABAQUS [64] input file. In the script, a rough optimization was implemented that optimizes the Young's moduli of the different elements so the elastic properties of a unit cell match the given elastic properties of a lamina. The recommended size of the unit cell is also provided by this algorithm. For our simulations, we initially wanted to generate the unit cells at the same density as our printed filaments in each ply, so each "fiber" in the discrete model would correspond to a filament in the specimen. This idea was soon abandoned as it would make the number of elements in the model extremely large, and simulations time prohibitively long. We also wanted to model the fiber elements using general beam cross-sections using filament measurements determined in our morphology study. This idea was also forced to be abandoned because the general cross section beam elements in ABAQUS required extensive additional work to implement in our current model, and the project time line did not allow us time to try and implement these required changes.

At the end, a compromise was made. We kept the unit cell size at a reasonable value (determined by the rough optimization algorithm in the input file generation script), and instead of a general shape cross sectional area, a rectangular cross sectional area was used for the fiber elements. The matrix, diagonal and inter-laminar elements were kept circular in cross section (default setting for the model), because they do not represent any tangible physical features in the 3D printed material, but were only simulating the physical interactions between the printed filaments.

For our simulations of the 3D printed tensile specimens, a unit cell size of 1.1428mm was used. The diameter of the non-fiber elements was 0.151mm, and the measurements for the fiber elements were H = 0.151mm, W = 0.3935mm, where W is the in-plane direction. The width and height of the fiber elements were measured in our morphology study of the new specimens (after the extruder change). The physical

properties to which we calibrated our models to match were also taken from the tensile tests of the new specimens.

6.2.1 Elastic Calibration

For the elastic calibration process, I started from the material moduli (each material used for its corresponding element in the discrete model) from the input file rough optimization results, and adjusted the materials manually to match the test results. The process can be summarized by the following steps:

1. Match the 0°experiment results by only changing the fiber property.

2. Using the updated 0°property, match the 90°experiment results by only changing the matrix property.

3. By adjusting both matrix and fiber properties slightly, match both the 0°and 90°results.

4. Using the updated properties, match the +-45°experiment results by changing the diagonal property.

5. Perform some final adjustments on all three material properties, until the simulations match all three experimental results.

Because the loading cases we were simulating were all in-plane tensile tests, the elastic modulus of the inter-laminar cohesive elements was not modified and was kept at the same value outputted by the input file generation code.

6.2.2 Strength Calibration

For the strength calibration, the process largely follows the same step as the elastic calibration, where it is a series of trial and errors. Unlike the elastic calibration,

a user defined material needed to be defined to include both the strength and the fracture energy of the material. In theory, by calibrating the strengths and energy of the materials in the discrete model, we should be able to match the non-linear behavior shown in the experiments at the structural level. However, due to the time constraint of this project, I only calibrated the strength values of the elements. The resulting model behaves in a linear fashion following the elastic calibration results, and the final stress values were calibrated to match the experimental values. This means that both the pre-peak and post-peak nonlinearity in our tensile test results were not captured by the model in its current configuration.

6.3 Model Calibration Results

The elastic calibration results of the model are shown in table 6.1. The stiffness of the elements were calculated using equation 6.4, where E is the elastic modulus of the element, A is the element cross sectional area and L is the element length.

$$k = \frac{EA}{L} \tag{6.4}$$

We can see from table 6.1b that our simulations were able to match the experimental values almost dead on. The final element stiffness values also intuitively made sense, as the fiber element stiffness is higher than that of the matrix and diagonal elements, but not by a couple magnitudes like you would expect in a fiber composite lamina. This is consistent with our tensile test results shown in chapter 5, where we have some anisotropy in terms of the elastic modulus based on specimen layup (print direction), but again, not to the same level as the anisotropy commonly displayed by fiber composite materials.

The strength calibration results are shown in table 6.2 and figure 6.3. Table 6.2 shows the material parameters for their respective type of element finalized in the strength calibration. Figure 6.3 visually compares the ultimate stress values achieved in simulations and in mechanical testings.

Finalized element properties	
Fiber material elastic modulus (MPa)	7500
Matrix material elastic modulus (MPa)	19000
Diagonal material elastic modulus (MPa)	10300
Fiber element stiffness (kN/m)	390.0
Matrix element stiffness (kN/m)	297.7
Diagonal element stiffness (kN/m)	161.4

(a)

Simulation results compared to experimental data			
Layup type	Simulated elastic modulus (MPa)	Experimental elastic modulus (MPa)	Error (%)
0°	3425.8	3397.2	-0.6082
+-45°	3007.0	3025.4	0.8419
90°	2841.3	2872.1	-1.072

(b)

Table 6.1: Elastic calibration results

Finalized element properties			
Material name	Elastic modulus (MPa)	Strength (MPa)	Energy (N/mm)
Fiber	7500	220	5
Matrix	19000	300	5
Diagonal	10300	250	5
Cohesive	10260	86	5

Table 6.2: Finalized element properties for strength calibration

We can see that just by altering the material strengths, we can already match the structural strength performances of actual tested specimens. However, in order to fully utilize the potential of the discrete model, further calibration and optimization of the energy parameter would need to be done. In all the simulations conducted for this thesis, the model behaves linearly until its failure, which does not capture the pre-peak and post-peak non-linear behavior of the real material. In theory, with the correct energy values, we should be able to replicate the structural behavior shown in experimental results from start to finish.

6.4 Model Prediction Results

To test the ability of the calibrated explicit model at predicting the mechanical properties of printing directions other than the ones tested, we simulated tensile specimens of two other layups. The additional layups simulated were +-10°+-20°, +-30°and +-50°. To test the accuracy of the simulated results, we compared the simulated elastic moduli to the ones calculated based on classical laminate theory (CLT) using lamina properties calculated from test results as shown in table 5.2. The comparison results are shown in table 6.3. As we can see, the Young's modulus prediction by the discrete model is very close to that predicted by the CLT (maximum error smaller than

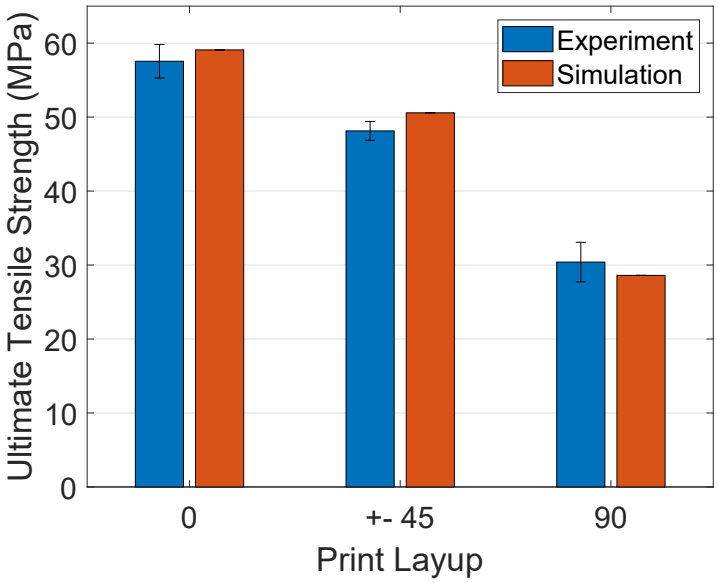

Figure 6.3: Strength calibration results compared to experimental data

5%), which further validates the capability of the discrete model at predicting the mechanical properties of FDM 3D printed materials once calibrated.

Printing direction(s)	CLT predicted E	Model predicted E	Difference
+-10°	3369.13 MPa	3533.10 MPa	4.75%
+-20°	3292.68 MPa	3106.40 MPa	3.08%
+-30°	3188.22 MPa	3106.40 MPa	2.60%
+-50°	2991.19 MPa	2947.40 MPa	1.47%

Table 6.3: Comparison between CLT and discrete model prediction of E

Chapter 7

CONCLUSION

The overarching goal of this study was to investigate the effects of the morphology on the mechanical behavior of parts made via Fused Deposition Modeling (FDM) and to utilize this knowledge to calibrate a novel discrete computational model. Based on the results obtained in this project, the following conclusions can be elaborated on the results and possible future steps to provide a well rounded computational framework for FDM.

7.1 Project Conclusion and Discussion

From this project, it is undeniable that more knowledge about FDM 3D printed material has been acquired. Reflecting on the targets set at the beginning of this project, we have successfully achieved most of the goals envisioned for this study.

In regard to the morphology analysis, we have successfully developed a fully in-house morphology analysis package, from which we were able to obtain definitive measurements of the overall morphology characteristics such as the total area of voids and void fraction from a micrograph image. In addition, the morphology package has also enabled us to algorithmically extract more detailed morphological measurements such as the area and shape of each and every individual void and filament (almost), rather than performing such measurements by hand, which can only be realistically done on a few selected voids or filaments. By obtaining these measurements for all the individual morphological features, we have been able to study the statistical distributions of these measurements and potentially see how they are affected when we alter printing parameters or machine configuration.

This information is quintessential to understand how the mesoscale morphology affects the mechanical behavior of parts made via FDM, which is a fundamental step towards the formulation of predictive computational models.

We have successfully performed all the essential mechanical tests required to characterize the performance of our material and to calibrate our FEM model. All the tests were conducted following ASTM standard guidelines whenever we could. Not only were we able to verify some of the previously investigated hypotheses such as the anisotropy of the FDM 3D printed material as a result of its inherent voids, the tests were also paramount in providing our group with a lot of useful first-hand knowledge and experience in manufacturing and testing using FDM 3D printed material. The tests were also essential in serving as the calibration goals of our FEM model and served as the physical representation of the combined effect of all the morphological characteristics analyzed and quantified in the morphology study.

In particular, our tests are the first to characterize the anisotropy of the fracture energy and the related size effects leveraging the work of fracture for various printing directions. This information is of paramount importance for the calibration and validation of computational models as well as the formulation of proper design guidelines that account for the different fracture behavior as a function of the printing direction and parameters.

In terms of the numerical modeling aspect of our project, while our preliminary results have validated the viability of our discrete model to be used for modeling FDM 3D-printed material, we may have only scratched the surface in terms of exploring the potential of the discrete model for its application on FDM 3D-printed material. According to the preliminary results, we can conclude that it would be possible to achieve a better match of the material behavior with further calibrations of our existing model.

Overall, the results and findings accomplished in this project have paved a concrete foundation for future studies that our lab plans to conduct in this area, and act as a

corner stone in realizing our vision of developing a complete FDM design guideline.

Our main findings and achievements can be summarized as follows:

Morphology:

- From morphology studies, we have identified void shapes that were not previously discussed and proposed a new characteristic shape to characterize their morphology;

- We successfully developed a cross-section morphology characterization code for FDM 3D printed material that can identify and analyze all the characteristic void shapes we have identified;

- Leveraging the novel code for morphological analysis, we saw a significant change in cross-section morphology of the printed material following an extruder change. By comparing the morphology results before and after the extruder change, we can see a decrease in void fraction by approximately 36%. A decrease in standard deviation of void areas by approximately 55% was also observed. From these results, we can conclude that the characteristics of the extruder have a great effect on the overall print quality;

- Combined with mechanical testing results, we can conclude that for FDM 3D printed materials, there is a strong correlation between the reduction in void fraction and the gains in strength and toughness.

Tensile tests:

- From tensile testing results, we were able to observe that the difference in Young's modulus between the highest (0°) and the lowest (90°) values was around 15.5%. The strength discrepancy between the strongest (0°) and the

weakest specimens (90°) was around 47%. The approximate difference in maximum strain between the most brittle specimens (90°) and the toughest specimens (+-45°) was a staggering 80.4%;

- From these tensile testing results, we can see a moderate anisotropy in the linear elastic region across the printing direction spectrum. In terms of strength, we can see a much more significant discrepancy between different printing directions. However, the most significant anisotropy between different printing directions is in the level of post peak plasticity (maximum strain). This suggests that in designs using the FDM 3D printed materials, the limiting factors in selecting printing directions are more likely to be the resulting strength and toughness;

- Our tensile testing results are different from that

Single Edge Notched Bending (SENB) tests:

- From SENB testings of three different layups and two different sizes, we have observed plastic fracture behavior in all the specimens that we tested. This means that the majority of the energy dissipated during the fracture of FDM 3D printed PLA will be captured in the form of plastic deformation;

- We have also observed a clear size effect in the 0°and +-45°SENB specimens where the fracture energy of the larger specimens were significantly higher than that of the smaller specimens. This remarkable size effect implies that the size of the end-use structure should be taken into consideration in future designs using FDM 3D printed materials;

- Similar size effect has been observed on FDM 3D printed acrylic resin by Siegmund et al. [65], where the researchers observed an increase in fracture toughness with increasing specimen size. However, our testing results have shown

that not only does the fracture energy of FDM 3D printed PLA increase with specimen size, the level of this size effect is also different for each printing directions. This suggests that the level of size effect in FDM 3D printed PLA is anisotropic and is a function of printing directions.

Numerical modeling using FastDM4C discrete model:

- In terms of numerical modeling, we have confirmed in our elastic calibration results, that the FastDM4C model developed by MAMS is capable of accurately capturing the elastic behavior of FDM 3D printed materials with different printing directions;

- We saw that once calibrated, the FastDM4C model was able to predict the elastic modulus resulting from different printing directions;

- We have also verified that the FastDM4C model is able to capture the anisotropy in strength of FDM 3D printed materials as a function of different printing directions. Further calibrations of the constitutive element properties for our model will be required to fully capture the mechanical behaviors of FDM 3D printed materials, including their pre-peak and post-peak non-linearity that followed the linear-elastic region shown in our experimental results.

7.2 Future Steps Towards Completing the FDM Design Guideline

Following this project, future work should primarily focus on two aspects. The first one would be to further calibrate the discrete model, with emphasis in capturing the pre-peak and post-peak non linear behavior of the material. At the end of the day, we would like to have a robust modeling tool that once calibrated for a material, can be used to predict mechanical performances of any structure manufactured with said material. This will require the implementation of elasto-plastic constitutive equations

aimed at capturing the large irreversible nonlinear behavior typical of thermoplastic composites.

The second aspect that should be an emphasis would be to further investigate the effect of printing parameters on the cross section morphology of the resulting printed material. With the morphology analysis package already developed and validated, future work should focus on analyzing the cross section morphology of materials manufactured using printing parameters other different from the ones used in this thesis.

Due to the limited time of this thesis, only the most basic morphological measurements such as the area and moment of inertia were calculated from the morphology analysis results. More detailed morphological measurements should be one of the targets of future work, so we can establish a better understanding in how the morphology of the printed material changes as a function of printing parameters by examining the correlations between printing parameters and these more detailed morphological measurements.

Finally, it would be important to verify how many of the conclusions made in this thesis are valid for FDM printed parts made from different feedstock materials with different bulk characteristics to PLA. Types of material that should be investigated include but not limited to high-strength semi-crystaline polymers such as PEEK, plastics reinforced with different types of inorganic fillers such as chopped carbon/glass fiber and graphene nanoplatelet, even organic bio-fillers such as algae and bacteria cellulose.

BIBLIOGRAPHY

[1] T.D. Ngo, A. Kashani, G. Imbalzano, K.TQ. Nguyen, and D. Hui. Additive manufacturing (3-D printing): A review of materials, methods, applications and challenges. *Composites Part B: Engineering*, 143:172–196, 2018.

[2] C.W. Hull. Apparatus for Production of Tthree-Dimensional Objects by Stereolithography. *United States Patent, Appl., No. 638905, Filed*, 1984.

[3] S.A. Tronvoll, T. Welo, and C.W. Elverum. The effects of voids on structural properties of fused deposition modelled parts: A probabilistic approach. *The International Journal of Advanced Manufacturing Technology*, 97(9):3607–3618, 2018.

[4] T. Wohlers and T. Gornet. History of Additive Manufacturing. *Wohlers report*, page 118, 2016.

[5] M. Attaran. The rise of 3-D printing: The advantages of additive manufacturing over traditional manufacturing. *Business Horizons*, 60(5):677–688, 2017.

[6] P. Wang, B. Zou, S. Ding, L. Li, and C. Huang. Effects of FDM-3D printing parameters on mechanical properties and microstructure of CF/PEEK and GF/PEEK. *Chinese Journal of Aeronautics*, 34(9):236–246, 2021.

[7] H. Cui, M. Nowicki, J.P. Fisher, and L.G. Zhang. 3D bioprinting for organ regeneration. *Advanced healthcare materials*, 6(1):1601118, 2017.

[8] J. Shah, B. Snider, T. Clarke, S. Kozutsky, M. Lacki, and A. Hosseini. Large-scale 3D printers for additive manufacturing: design considerations and challenges. *The International Journal of Advanced Manufacturing Technology*, 104(9):3679–3693, 2019.

[9] S.-H. Ahn, M. Montero, D. Odell, S. Roundy, and P.K. Wright. Anisotropic material properties of fused deposition modeling abs. *Rapid prototyping journal*, 2002.

[10] J.F. Rodriguez, J.P. Thomas, and J.E. Renaud. Characterization of the mesostructure of fused-deposition acrylonitrile-butadiene-styrene materials. *Rapid Prototyping Journal*, 2000.

[11] H. Fabritius, C. Sachs, D. Raabe, S. Nikolov, M. Friák, and J. Neugebauer. Chitin in the exoskeletons of arthropoda: From ancient design to novel materials science. In *Chitin*, pages 35–60. Springer, 2011.

[12] C. Mo and J.R. Raney. Spatial programming of defect distributions to enhance material failure characteristics. *Extreme Mechanics Letters*, 34:100598, 2020.

[13] N. Suksangpanya, N.A. Yaraghi, R.B. Pipes, D. Kisailus, and P. Zavattieri. Crack twisting and toughening strategies in Bouligand architectures. *International Journal of Solids and Structures*, 150:83–106, 2018.

[14] S. Garzon-Hernandez, D. Garcia-Gonzalez, A. Jérusalem, and A. Arias. Design of FDM 3D printed polymers: An experimental-modelling methodology for the prediction of mechanical properties. *Materials & Design*, 188:108414, 2020.

[15] M. Somireddy, A. Czekanski, and C.V. Singh. Development of constitutive material model of 3d printed structure via FDM. *Materials Today Communications*, 15:143–152, 2018.

[16] Print quality guide. *Simplify3D Software*, Jun 2019.

[17] ASTM D638-14. Standard test method for tensile properties of plastics. ASTM International, West Conshohocken, PA, 2014.

[18] ASTM D5045-14. Standard Test Methods for Plane-Strain Fracture Toughness and Strain Energy Release Rate of Plastic Materials. ASTM International, West Conshohocken, PA, 2014.

[19] C.H. Mefford, Y. Qiao, and M. Salviato. Failure behavior and scaling of graphene nanocomposites. *Composite Structures*, 176:961–972, 2017.

[20] T.C. Chu, W.F. Ranson, and M.A. Sutton. Applications of digital-image-correlation techniques to experimental mechanics. *Experimental mechanics*, 25(3):232–244, 1985.

[21] ASTM D3039/D3039M-17. Standard Test Method for Tensile Properties of Polymer Matrix Composite Materials. ASTM International, West Conshohocken, PA, 2017.

[22] ASTM D3518/D3518M-18. Standard Test Method for In-Plane Shear Response of Polymer Matrix Composite Materials by Tensile Test of a ±45°Laminate. ASTM International, West Conshohocken, PA, 2018.

[23] http://www.ncorr.com/.

[24] M.S. Cayard and W.L. Bradley. The effect of various precracking techniques on the fracture toughness of plastics. *ICF 7. Advances in Fracture Research.*, 4:2713–2723, 1989.

[25] A. Hillerborg. The theoretical basis of a method to determine the fracture energy G_F of concrete. *Materials and structures*, 18(4):291–296, 1985.

[26] L. Li, C. Bellehumeur, Q. Sun, and P. Gu. Composite modeling and analysis of FDM prototypes for design and fabrication of functionally graded parts. 2001.

[27] J. Wang, H. Xie, Z. Weng, T. Senthil, and L. Wu. A novel approach to improve mechanical properties of parts fabricated by fused deposition modeling. *Materials & Design*, 105:152–159, 2016.

[28] A. Nasirov, A. Gupta, S. Hasanov, and I. Fidan. Three-scale asymptotic homogenization of short fiber reinforced additively manufactured polymer composites. *Composites Part B: Engineering*, 202:108269, 2020.

[29] S. Yu, YH. Hwang, JY. Hwang, and SH. Hong. Analytical study on the 3D-printed structure and mechanical properties of basalt fiber-reinforced PLA composites using X-ray microscopy. *Composites Science and Technology*, 175:18–27, 2019.

[30] Matlab Documentation. *MathWorks*.

[31] J.N. Kutz. *Data-Driven Modeling & Scientific Computation: Methods for Complex Systems & Big Data*. Oxford University Press, 2013.

[32] S. Wold, K Esbensen, and P Geladi. Principal component analysis. *Chemometrics and intelligent laboratory systems*, 2(1-3):37–52, 1987.

[33] Z.P. Bažant, J.L. Le, and M. Salviato. *Quasibrittle Fracture Mechanics and Size Effect: A First Course*. Oxford University Press, 2021.

[34] C. Ceccato, M. Salviato, C. Pellegrino, and G. Cusatis. Simulation of concrete failure and fiber reinforced polymer fracture in confined columns with different cross sectional shape. *International Journal of Solids and Structures*, 108:216–229, 2017.

[35] M. Salviato, K. Kirane, Z.P. Bažant, and G. Cusatis. Mode I and II interlaminar fracture in laminated composites: a size effect study. *Journal of Applied Mechanics*, 86(9), 2019.

[36] Y. Qiao, A.A. Deleo, and M. Salviato. A study on the multi-axial fatigue failure behavior of notched composite laminates. *Composites Part A: Applied Science and Manufacturing*, 127:105640, 2019.

[37] Y. Qiao and M. Salviato. Micro-computed tomography analysis of damage in notched composite laminates under multi-axial fatigue. *Composites Part B: Engineering*, 187:107789, 2020.

[38] M. Salviato, K. Kirane, S.E. Ashari, Z.P. Bažant, and G. Cusatis. Experimental and numerical investigation of intra-laminar energy dissipation and size effect in two-dimensional textile composites. *Composites Science and Technology*, 135:67–75, 2016.

[39] M. Salviato, V.T. Chau, W. Li, Z.P. Bažant, and G. Cusatis. Direct testing of gadual postpeak softening of fracture specimens of fiber composites stabilized by enhanced grip stiffness and mass. *Journal of Applied Mechanics*, 83(11), 2016.

[40] K. Kirane, M. Salviato, and Z.P. Bažant. Microplane triad model for simple and accurate prediction of orthotropic elastic constants of woven fabric composites. *Journal of Composite Materials*, 50(9):1247–1260, 2016.

[41] M. Salviato, S.E. Ashari, and G. Cusatis. Spectral stiffness microplane model for damage and fracture of textile composites. *Composite Structures*, 137:170–184, 2016.

[42] K. Kirane, M. Salviato, and journal=Journal of Applied Mechanics volume=83 number=4 year=2016 publisher=American Society of Mechanical Engineers Digital Collection Bažant, Z.P. Microplane-triad model for elastic and fracturing behavior of woven composites.

[43] W. Li, Y. Qiao, J. Fenner, K. Warren, M. Salviato, Z.P. Bažant, and G. Cusatis. Elastic and fracture behavior of three-dimensional ply-to-ply angle interlock woven composites: Through-thickness, size effect, and multiaxial tests. *Composites Part C: Open Access*, 4:100098, 2021.

[44] S. Ko, J. Yang, M.E. Tuttle, and M. Salviato. Effect of the platelet size on the fracturing behavior and size effect of discontinuous fiber composite structures. *Composite Structures*, 227:111245, 2019.

[45] S. Ko, J. Davey, S. Douglass, J. Yang, M.E. Tuttle, and M. Salviato. Effect of the thickness on the fracturing behavior of discontinuous fiber composite structures. *Composites Part A: Applied Science and Manufacturing*, 125:105520, 2019.

[46] M. Zappalorto, M. Salviato, and M. Quaresimin. Influence of the interphase zone on the nanoparticle debonding stress. *Composites Science and Technology*, 72(1):49–55, 2011.

[47] M Quaresimin, M Salviato, and M Zappalorto. A multi-scale and multi-mechanism approach for the fracture toughness assessment of polymer nanocomposites. *Composites Science and Technology*, 91:16–21, 2014.

[48] Y. Qiao and M. Salviato. Strength and cohesive behavior of thermoset polymers at the microscale: A size-effect study. *Engineering Fracture Mechanics*, 213:100–117, 2019.

[49] Y. Qiao and M. Salviato. Study of the fracturing behavior of thermoset polymer nanocomposites via cohesive zone modeling. *Composite Structures*, 220:127–147, 2019.

[50] M. Zappalorto, M. Salviato, and M. Quaresimin. Assessment of debonding-induced toughening in nanocomposites. *Procedia Engineering*, 10:2973–2978, 2011.

[51] M. Salviato, M. Zappalorto, and M. Quaresimin. The effect of surface stresses on the critical debonding stress around nanoparticles. *International journal of fracture*, 172(1):97–103, 2011.

[52] M. Zappalorto, M. Salviato, and M. Quaresimin. A multiscale model to describe nanocomposite fracture toughness enhancement by the plastic yielding of nanovoids. *Composites Science and Technology*, 72(14):1683–1691, 2012.

[53] M. Zappalorto, M. Salviato, and M. Quaresimin. Stress distributions around rigid nanoparticles. *International Journal of Fracture*, 176(1):105–112, 2012.

[54] M. Salviato, M. Zappalorto, and M. Quaresimin. Plastic shear bands and fracture toughness improvements of nanoparticle filled polymers: a multiscale analytical model. *Composites Part A: Applied Science and Manufacturing*, 48:144–152, 2013.

[55] M. Salviato, M. Zappalorto, and M. Quaresimin. Nanoparticle debonding strength: a comprehensive study on interfacial effects. *International Journal of Solids and Structures*, 50(20-21):3225–3232, 2013.

[56] Z.P. Bažant, M. Salviato, V.T. Chau, H. Viswanathan, and A. Zubelewicz. Why fracking works. *Journal of Applied Mechanics*, 81(10), 2014.

[57] W Li, C Jin, M Salviato, and G. Cusatis. Modeling of failure behavior of anisotropic shale using lattice discrete particle model. In *49th US Rock Mechanics/Geomechanics Symposium*. OnePetro, 2015.

[58] H.W. Lilliefors. On the Kolmogorov-Smirnov test for normality with mean and variance unknown. *Journal of the American statistical Association*, 62(318):399–402, 1967.

[59] W. Weibull. A statistical distribution function of wide applicability. *Journal of applied mechanics*, 18(3):293–297, 1951.

[60] E. Cuan-Urquizo, S. Yang, and A. Bhaskar. Mechanical characterisation of additively manufactured material having lattice microstructure. In *IOP Conference Series: Materials Science and Engineering*, volume 74, page 012004. IOP Publishing, 2015.

[61] M. Domingo-Espin, J.M. Puigoriol-Forcada, A.-A. Garcia-Granada, J. Llumà, S. Borros, and G. Reyes. Mechanical property characterization and simulation of fused deposition modeling Polycarbonate parts. *Materials & Design*, 83:670–677, 2015.

[62] A.A. Deleo. A Fast and Efficient Discrete Model for Composites (FastDM4C). 2020.

[63] Z.P. Bažant. Size effect in blunt fracture: concrete, rock, metal. *Journal of engineering mechanics*, 110(4):518–535, 1984.

[64] Abaqus Documentation. *Dassault Systèmes*.

[65] D. Bell and T. Siegmund. 3d-printed polymers exhibit a strength size effect. *Additive Manufacturing*, 21:658–665, 2018.

Appendix A

STATISTICAL FIGURES OF MORPHOLOGICAL MEASUREMENTS

Here are the statistical figures of the remaining morphological measurements mentioned in chapter 5.

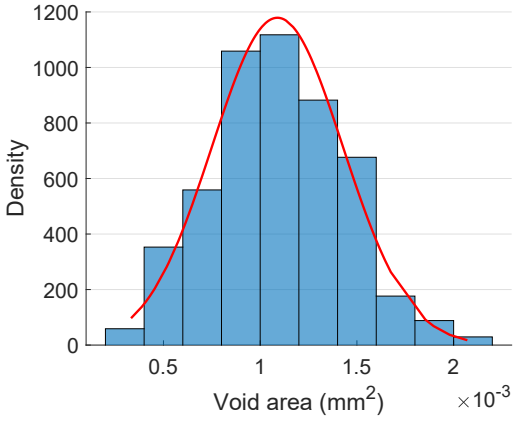

(a) Density histogram with fitted normal distribution curve

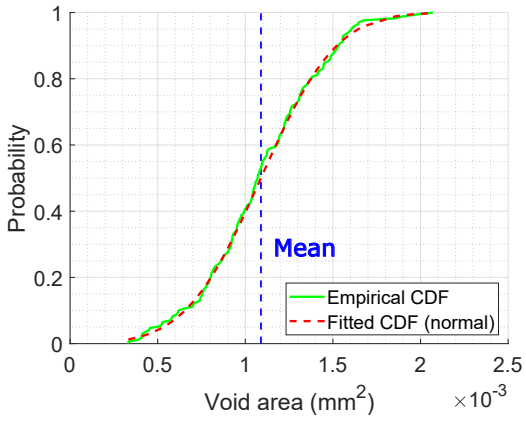

(b) Comparison between empirical CDF and fitted CDF

Figure A.1: Statistical figures of void area (A_v) (after extruder change)

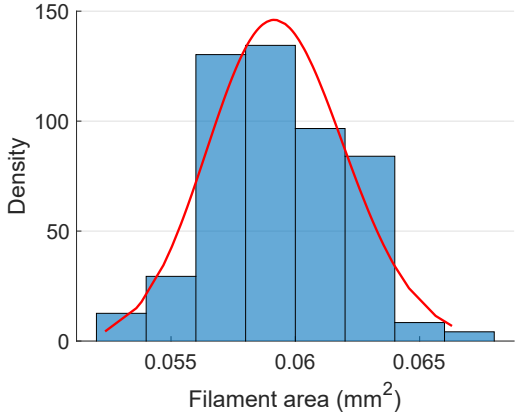

(a) Density histogram with fitted log-normal distribution curve

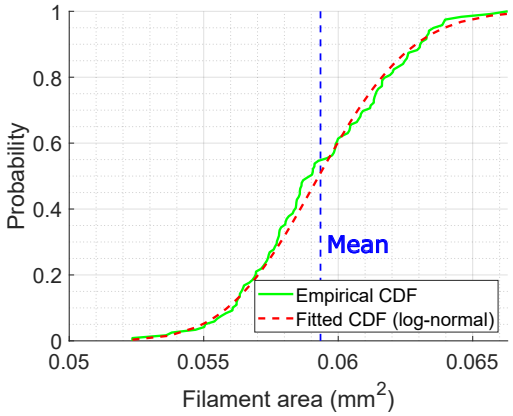

(b) Comparison between empirical CDF and fitted CDF

Figure A.2: Statistical figures of filament area (A_f) (after extruder change)

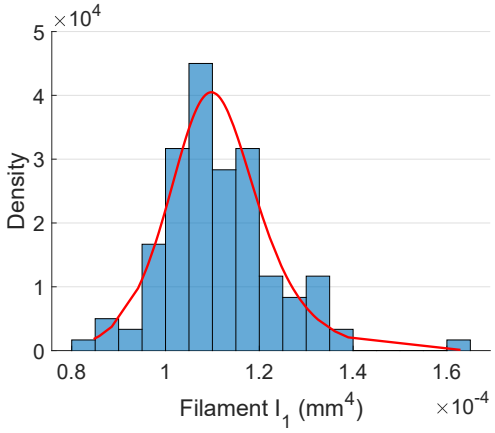

(a) Density histogram with fitted log-logistic distribution curve

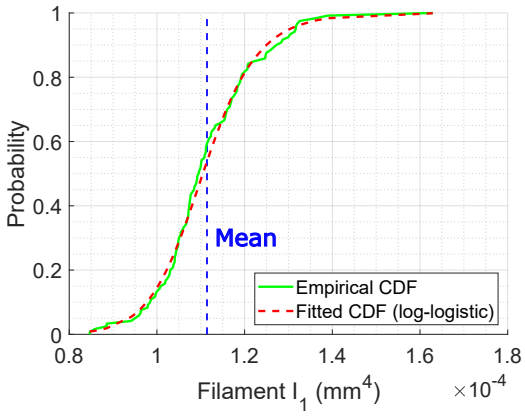

(b) Comparison between empirical CDF and fitted CDF

Figure A.3: Statistical figures of filament I_1 (after extruder change)

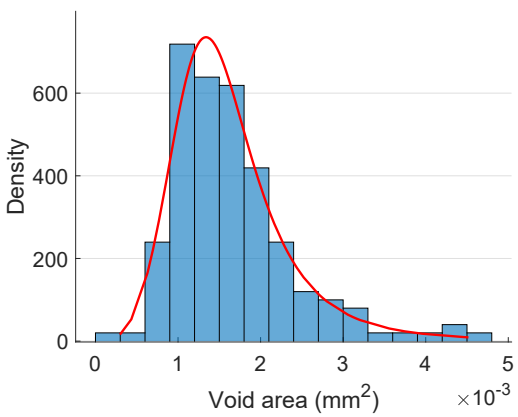

(a) Density histogram with fitted log-logistic distribution curve

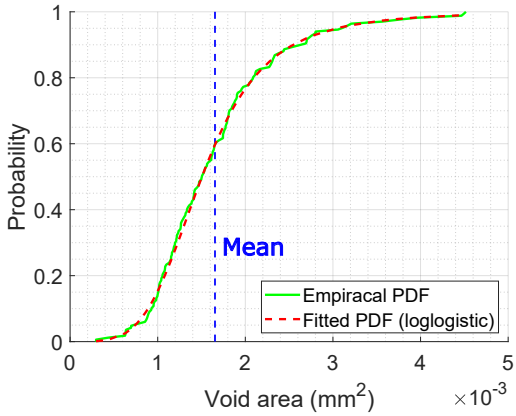

(b) Comparison between empirical CDF and fitted CDF

Figure A.4: Statistical figures of void area (A_v) (before extruder change)

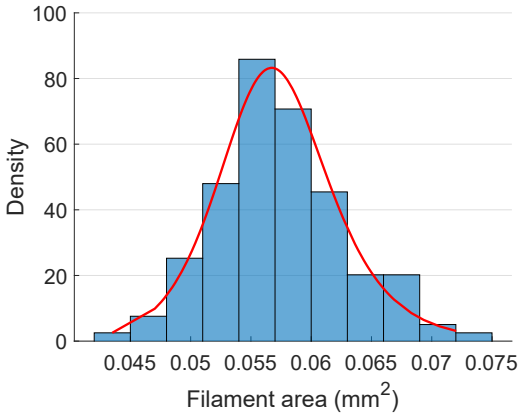

(a) Density histogram with fitted log-logistic distribution curve

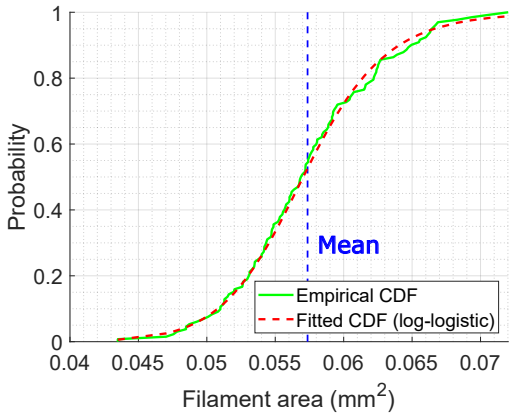

(b) Comparison between empirical CDF and fitted CDF

Figure A.5: Statistical figures of filament area (A_f) (before extruder change)

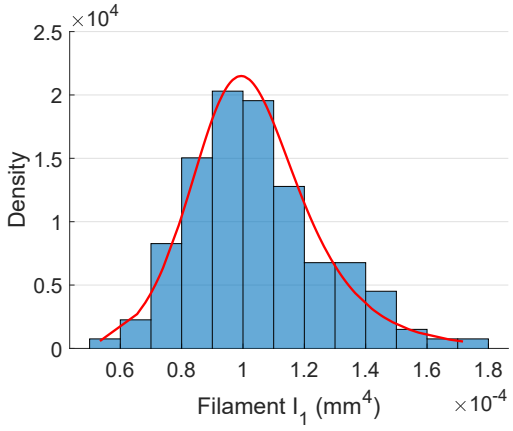

(a) Density histogram with fitted log-logistic distribution curve

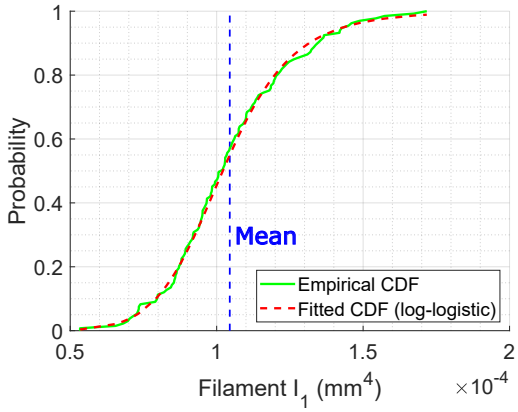

(b) Comparison between empirical CDF and fitted CDF

Figure A.6: Statistical figures of filament I_1 (before extruder change)

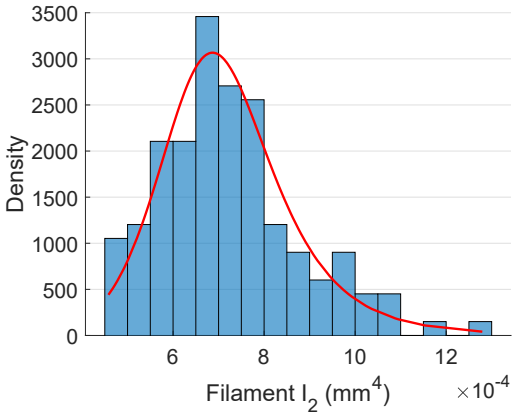

(a) Density histogram with fitted log-logistic distribution curve

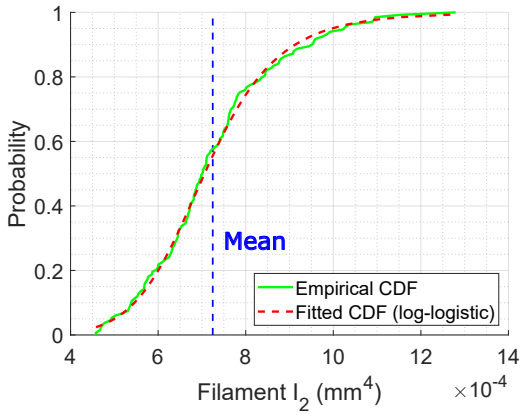

(b) Comparison between empirical CDF and fitted CDF

Figure A.7: Statistical figures of filament I_2 (before extruder change)